nature communications

Article

https://doi.org/10.1038/s41467-024-54827-5

A brain-to-liver signal mediates the inhibition of liver regeneration under chronic stress in mice

Received: 8 February 2024

Accepted: 21 November 2024

Yanyu Zhou[1,2,3], Xiaoqi Lin[1,2,3], Yingfu Jiao[1,2,3], Dan Yang[1,2,3], Zhengyu Li[1,2], Ling Zhu[1,2], Yixuan Li[1,2], Suqing Yin[1,2], Quanfu Li[1,2], Saihong Xu[1,2], Dan Tang[1,2], Song Zhang[1,2], Weifeng Yu[1,2] ✉, Po Gao[1,2] ✉ & Liqun Yang[1,2] ✉

As the ability of liver regeneration is pivotal for liver disease patients, it will be of high significance and importance to identify the missing piece of the jigsaw influencing the liver regeneration. Here, we report that chronic stress impairs the liver regeneration capacity after partial hepatectomy with increased mortality in male mice. Anatomical tracing and functional mapping identified a neural circuit from noradrenergic neurons in the locus coeruleus (LC) to serotonergic neurons in the rostral medullary raphe region (rMR), which critically contributes to the inhibition of liver regeneration under chronic stress. In addition, hepatic sympathetic nerves were shown to be critical for the inhibitory effects on liver regeneration by releasing norepinephrine (NE), which acts on adrenergic receptor β2 (ADRB2) to block the proinflammatory macrophage activation. Collectively, we reveal a "brain-to-liver" neural connection that mediates chronic stress-evoked deficits in liver regeneration, thus shedding important insights into hepatic disease therapy.

The liver has an outstanding regeneration potential, allowing itself to recover its original mass and maintain its function after an extensive hepatic tissue loss[1]. Liver regeneration process is deeply involved in several clinical conditions, including partial hepatectomy (PHx), severe chronic liver injury, metabolic liver diseases and liver fibrosis[2]. Despite this remarkable regenerative potential of the liver, a post-resection liver failure can occur in up to 9% of the cases, leading to a perioperative mortality rate of 45%[3]. The regenerative capacity of the liver is a key determinant for the recovery outcome from a hepatectomy, such as for malignancies or for living-donor liver transplantations[4]. Multiple factors and pathways have been shown to be important for the liver regeneration, including cytokines, growth factors, and metabolic networks[5]. Previous studies have been mainly focused on intrahepatic signaling pathways. However, the regulatory mechanisms of liver regeneration beyond the liver, especially the "brain-liver" signaling axis, still need to be explored.

Stress is a fundamental factor governing the adaptation of the human organism to dynamic internal and external environments[6]. It has been reported that eustress, which refers to the positive form of stress, promotes liver regeneration and anti-tumor immunotherapy effects[7,8]. Nevertheless, chronic and excessive stress can become detrimental to the body homeostasis[9]. Patients with chronic liver diseases, characterized by long duration, recurrent symptoms, and a high risk of malignancy, are often exposed to a state of chronic stress[10]. Moreover, several perioperative factors, such as preoperative anxiety, fasting, trauma, and postoperative pain, can lead to excessive stress, worsening the postoperative prognosis[11,12]. Consistently, population studies have also indicated that higher levels of psychological distress are associated with increased liver disease mortality rates[13]. However, whether and how chronic stress affects liver regeneration remains mysterious.

It is well known that brain is one of the most sensitive organs in response to chronic stress. This prompt stress response is regulated by

---

[1]Department of Anesthesiology, Renji Hospital, Shanghai Jiao Tong University School of Medicine, Shanghai 200127, China. [2]Key Laboratory of Anesthesiology (Shanghai Jiao Tong University), Ministry of Education, Shanghai, China. [3]These authors contributed equally: Yanyu Zhou, Xiaoqi Lin, Yingfu Jiao, Dan Yang. ✉e-mail: ywf808@yeah.net; gaopo0908@163.com; lqyang72721@126.com

a variety of brain regions involving the limbic forebrain, hypothalamus, and brainstem, which control the autonomic nervous and neuroendocrine systems[14]. Notably, previous studies have revealed that hypothalamic neurons are linked to the liver regeneration process following PHx[15,16]. However, limitations in tracing tools and strategies for targeted manipulation of liver-innervating neurons have prevented a clear understanding of the precise cell type and neural circuit in the "brain–liver" axis.

In this study, we combined viral tracing, electrophysiological recording, chemogenetic manipulation, and flow cytometry analysis to uncover the central neural circuit mechanism that regulates liver regeneration under chronic stress, as well as their interaction through the "brain-liver" axis. We identified a neural connection from the locus coeruleus (LC) to the rostral medullary raphe region (rMR), and then to the hepatic sympathetic nerves, which could block the proinflammatory macrophage activation through releasing norepinephrine (NE). The elucidation of these mechanisms helps to improve liver regeneration ability, thereby improving the prognosis of patients with chronic liver disease.

Results

Chronic stress inhibits liver regeneration after PHx

To investigate the effects of chronic stress on liver regeneration after PHx, we first generated a chronic sleep deprivation (CSD) mouse model, mimicking the sleep loss and anxiety state in clinical populations (Fig. 1a). After 21 days of exposure, behavioral tests indicated that CSD led to an increased anxiety state in the mice, as shown by the reduced time spent in the central area of the open field test (OFT) (Fig. 1b, c) and the decreased exploration of the open arms in the elevated plus maze (EPM) test (Supplementary Fig. 1). After CSD, mice were subjected to 90% PHx. The results showed that the overall survival rate of the CSD+PHx mice was significantly lower than that of the PHx mice (Fig. 1d). Moreover, 70% PHx was performed on mice after CSD, which represents the most commonly used model for the study of liver regeneration. We found that the liver mass and the liver/body weight ratio were both lower in CSD mice than those in naive mice at 48 and 72 hours after the PHx (Fig. 1e, f). This result was also confirmed by Ki67 (the hepatocyte proliferation marker) immunohistochemistry staining (Supplementary Fig. 2). Additionally, the expression levels of the *Ki67* and proliferating cell nuclear antigen (*Pcna*) were all significantly decreased at 48 hours after PHx in the CSD mice (Fig. 1g-l).

We next asked whether chronic stress-induced impairment in liver regeneration could be recapitulated in other animal models. As illustrated in Supplementary Fig. 3a-d, chronic restraint stress (CRS) induced anxiety-like behaviors accompanied by a significant decrease in the liver/body weight ratio. Moreover, the gene and protein expression levels of *Ki67* and *Pcna* were also decreased in CRS+PHx mice compared to the PHx mice (Supplementary Fig. 3e-j). Taken together, these results indicate that chronic stress inhibits liver regeneration after PHx.

NE^{LC}–5-HT^{rMR} neural circuit lies in neural pathways innervating the liver

To dissect the neural mechanisms underlying chronic stress-induced deficits in liver regeneration, we first traced the neural circuit connecting the brain and liver by injecting a fluorescent protein-expressing recombinant pseudo-rabies virus (PRV) into the mouse liver. After approximately 6 days, the PRV was shown to have reached the brain. Notably, in the brainstem, the locus coeruleus (LC) was prominently labeled (Supplementary Fig. 4d). LC contains a "tube-like" collection of noradrenergic neurons (NE neurons) and plays an important role in regulating stress response[17,18]. To clarify whether the NE neurons of LC innervate the liver, immunofluorescent staining of brain slices from PRV-injected mice was performed with an antibody recognizing tyrosine hydroxylase (TH), a rate-limiting enzyme that catalyzes the biosynthesis of NE[19] (Fig. 2a, b). We found that a large portion of PRV-labeled neurons in the LC were NE neurons (43.86% $EGFP^+$ neurons were TH^+ neurons and 35.44% TH^+ neurons were $EGFP^+$ neurons) (Fig. 2c). Moreover, the neurons of the rostral medullary raphe region (rMR, a key sympathetic center) were also densely labeled by PRV (Fig. 2d). The rMR consists of the rostral raphe pallidus nucleus (rRPa) and the raphe magnus nucleus (RMg), which are mainly populated with the sympathetic premotor neurons[20]. Sympathetic premotor neurons can directly project to the intermediolateral cell column (IML) of the thoracic spinal cord, which is then connected to peripheral sympathetic ganglia (SG)[21]. To identify the rMR neuron subtype labeled by the PRV, we focused on two previously reported neuron types: serotonin (5-HT) positive neurons and the G protein-coupled estrogen receptor (GPER) positive neurons[22]. Confocal microscopy images showed that PRV-labeled neurons in the rMR were mainly co-localized with 5-HT rather than with GPER (Fig. 2e and Supplementary Fig. 4j).

To clarify whether NE^{LC} neurons can project to rMR, we used *Cre*-dependent retrograde adeno-associated virus (AAV) in *Th-Cre* mice. We injected a *Cre*-dependent retrograde AAV2 carrying recombinase flippase (FLP) vector into the rMR and *Flp*-dependent AAV (AAV-fDIO-EGFP) into the LC, which could make the rMR-projecting NE^{LC} neurons express green fluorescence signals (Fig. 2f). The results showed that NE^{LC} neurons from different dimensions could project to the rMR, and most of them come from the tail region of LC (Fig. 2g, h). Moreover, to investigate the relationship between the rMR-projecting NE^{LC} neurons and the neurons innervating the liver, we first injected the *Cre*-dependent retrograde AAV2 carrying recombinase FLP vector into the rMR, and the *Flp*-dependent AAV (AAV-fDIO-mCherry) into the LC. Three weeks later, we injected PRV-CAG-EGFP into the liver, to trace the liver-innervating LC neurons (Fig. 2i). We found that about 46.45% of the co-labeled neurons were TH^+/$mCherry^+$ neurons, and 54.87% of the co-labeled neurons were TH^+/$EGFP^+$ neurons (Fig. 2j-l), indicating that the rMR-projecting NE^{LC} neurons are the same subgroup as the NE^{LC} neurons innervating the liver.

To determine the specific neuronal type of the rMR that receives the innervation from the LC, we performed an anterograde trans-synaptic tracing assay by injecting AAV2/1-Cre into the LC and AAV2/9-DIO-mCherry into the rMR, enabling selective mCherry expression in LC-innervated rMR neurons (Supplementary Fig. 5a). The results revealed that most mCherry positive neurons were co-labeled with 5-HT (Supplementary Fig. 5b), indicating that the 5-HT^{rMR} neurons were the downstream target of LC neurons. Conversely, we used *Pet1-Cre* mice, a mouse line that expresses the Cre enzyme in 5-HT neurons[23], to investigate whether the upstream of 5-HT^{rMR} neurons is NE^{LC} neurons. Rabies virus (RV)-mediated retrograde tracing from 5-HT^{rMR} neurons was performed to confirm the synaptic relay of the LC-rMR neural connection (Fig. 2m). Starter cells were identified as $EGFP^+$/$mCherry^+$ double-positive neurons (Fig. 2n). The neurons retrogradely labelled by EGFP were identified in LC (Fig. 2o). There were 48.97% of $EGFP^+$/TH^+ neurons in $EGFP^+$ neurons and 25.12% of those in TH^+ neurons (Fig. 2p, q). Additionally, to verify the functional connection from NE^{LC} neurons to 5-HT^{rMR} neurons, we activated rMR-projecting NE^{LC} neurons optogenetically and recorded the changes in calcium signals of 5-HT^{rMR} neurons using fiber photometry. Specifically, we injected AAV2/9-fDIO-ChrimsonR-mCherry into the LC and meanwhile the retrograde AAV carrying recombinase FLP vector with TH promoters was injected into the rMR, which allowed rMR-projecting NE^{LC} neurons to express ChrimsonR-mCherry. Moreover, the AAV-DIO-GCaMP8s was injected into the rMR of *Pet1-Cre* mice (Fig. 2r). Immunostaining results showed that most neurons expressing GCaMP8s are 5-HT positive neurons in the rMR (Supplementary Fig. 5c). Fiber photometry recording results showed that optogenetic activation of rMR-projecting NE^{LC} neurons could induce a rapid increase in calcium signaling of 5-HT^{rMR} neurons (Fig. 2s, t),

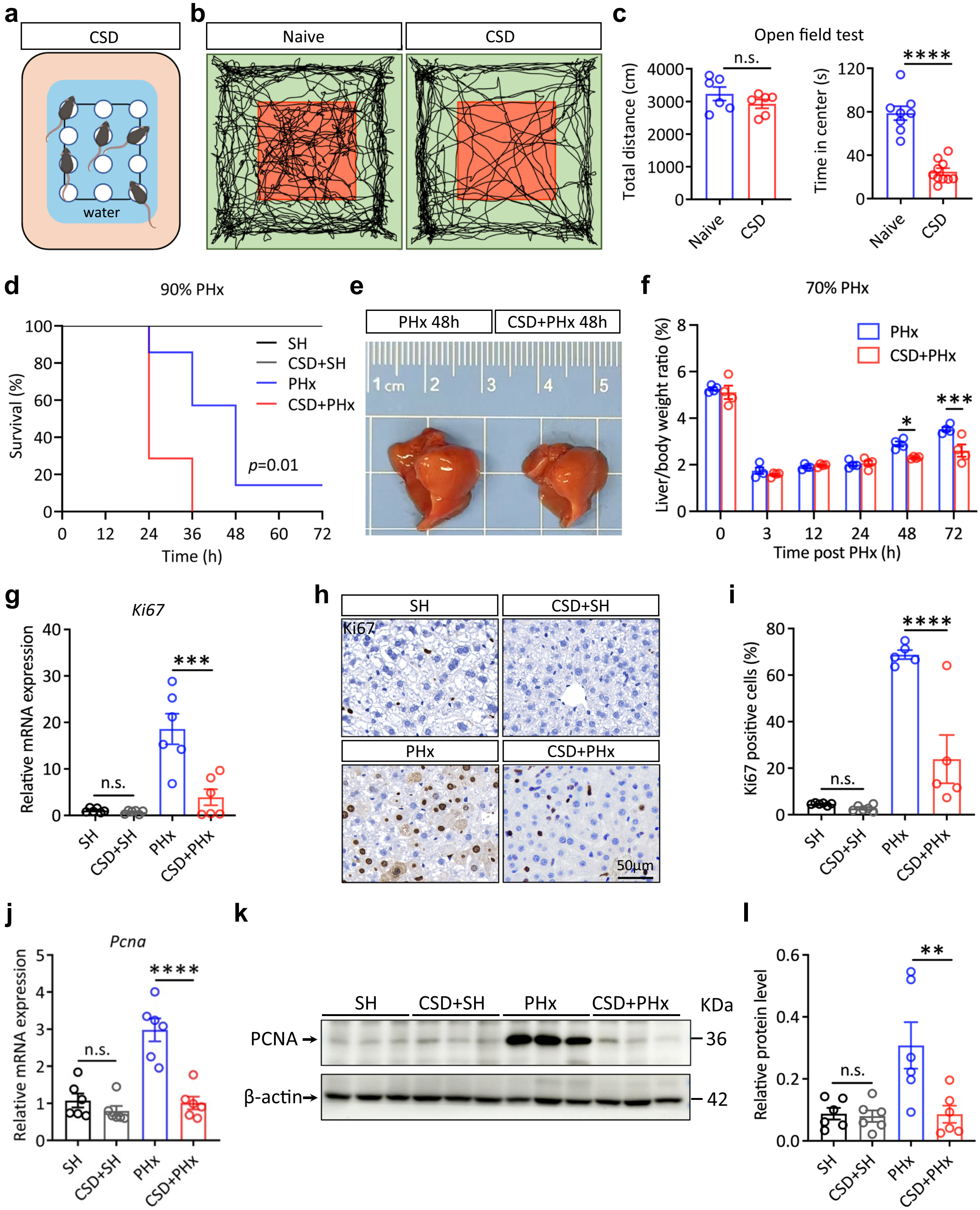

indicating a clear functional connection between NE^{LC} neurons and 5-HT^{rMR} neurons. Moreover, we chemogenetically activated the rMR-projecting NE^{LC} neurons in *Th-Cre* mice (Supplementary Fig. 5d). Results revealed that 5-HT^{rMR} neurons were markedly activated by the administration of the hM3Dq agonist clozapine N-oxide (CNO) (Supplementary Fig. 5e, f). Together, these findings demonstrate that the NE^{LC} neurons can project to the 5-HT^{rMR} neurons.

The NE^{LC}-5-HT^{rMR} neural circuit is activated under chronic stress

To characterize the activity of the NE^{LC}-5-HT^{rMR} neural circuit under chronic stress, we first examined the expression of c-Fos (a neuronal activity marker) in NE^{LC} neurons of CSD mice. We observed a significant increase in the number of TH^{+}/c-Fos^{+} neurons under the CSD condition (Supplementary Fig. 6a, b). Furthermore, we measured the activation of rMR-projecting NE^{LC} neurons. To this end, the *Cre*-

Fig. 1 | Chronic sleep deprivation impairs liver regeneration after PHx. **a** Schematic diagram of the chronic sleep deprivation (CSD) experimental model. Representative track map of the open field test (OFT) in naive and CSD mice (**b**). Mice in both groups traveled similar distances ($n = 6$ mice) n.s. $p = 0.2417$; however, CSD mice spent significantly less time in the center of the open field (**c**) ($n = 8$ and 10 mice, respectively) $^{****}p < 0.0001$. **d** Survival curve of SH, CSD + SH, PHx and CSD +PHx mice in response to a lethal 90% PHx ($n = 9$, 9, 9 and 7 mice, respectively). The overall survival rate of CSD+PHx mice was significantly lower than that of PHx mice. SH, Sham. **e** Representative liver tissue images collected at 48 hours after 70% PHx, in naive mice (left) and in CSD mice (right). **f** In comparison with naive mice, the liver/body weight ratio of CSD mice was significantly lower at 48 and 72 hours after 70% PHx ($n = 4$ mice) $^{*}p = 0.0262$, $^{***}p = 0.0002$. **g** *Ki67* mRNA expression levels were decreased in CSD mice at 48 hours after 70% PHx ($n = 6$ mice) n.s. $p = 0.9992$, $^{***}p = 0.0001$. Representative immunohistochemistry (IHC) staining image (**h**) and quantification (**i**) of Ki67 positive cells in liver sections in each group of mice ($n = 6$, 6, 5 and 5 mice, respectively) n.s. $p = 0.9999$, $^{****}p < 0.0001$. **j** *Pcna* mRNA expression levels were decreased in CSD mice at 48 hours after 70% PHx ($n = 6$ mice) n.s. $p = 0.7833$, $^{****}p < 0.0001$. Representative western blot images (**k**) and quantification (**l**) of the PCNA protein expression levels in the liver tissues for each group of mice ($n = 6$ mice) n.s. $p = 0.9991$, $^{****}p < 0.0001$. Two-tailed unpaired *t* test (**c**); log-rank test (**d**); two-way ANOVA (**f**); one-way ANOVA (**g, i, j** and **l**). Data are presented as mean ± SEM. Source data are provided as a Source Data file. **a** was created in BioRender. Zhou, Y. (2024) https://BioRender.com/m36w172.

dependent retrograde AAV2 carrying recombinase FLP vector was injected into the rMR and the AAV-fDIO-EGFP virus was injected into the LC, which allowed rMR-projecting NE^{LC} neurons to express green fluorescence signals (Fig. 3a). The coimmunostaining results showed that the percentage of c-Fos^{+}/$EGFP^{+}$/TH^{+} neurons among $EGFP^{+}$/TH^{+} neurons was approximately 40% in CSD mice, which was significantly higher than that in naive mice (Fig. 3b, c).

Next, whole-cell patch-clamp recordings were applied to detect the excitability of the LC-rMR neural circuit. Three weeks after the retrograde AAV injection, EGFP-positive neurons were selected for patch-clamp recordings (Fig. 3d), and the recorded neurons were identified as NEergic by biocytin labeling (Fig. 3e). We found that rMR-projecting NE^{LC} neurons from CSD mice exhibited a relatively depolarized resting membrane potential and smaller threshold current to elicit action potentials (APs) compared to those from the naive mice (Fig. 3f-h). Consequently, the firing rate of APs evoked by the step current injection was dramatically increased (Fig. 3i, j). Furthermore, both the frequency and amplitude of spontaneous excitatory postsynaptic currents (sEPSCs) were significantly higher for NE^{LC} neurons from CSD mice than those from the naive mice (Fig. 3k-m). These data support the notion that both intrinsic excitability and synaptic transmission efficacy of the rMR-projecting NE^{LC} neurons were considerably enhanced under chronic stress conditions.

To clarify whether NE^{LC} neurons lying in the neural pathways innervating liver are activated under CSD condition, the PRV-CAG-EGFP was injected into the livers of CSD mice and continuously administered stress. The results showed that the proportion of TH^{+}/$EGFP^{+}$/c-Fos^{+} neurons in the LC of CSD mice was significantly higher than that of naive mice (Supplementary Fig. 6c, d).

Finally, immunostaining results showed that the proportion of c-Fos^{+}/5-HT^{+} neurons in rMR was significantly increased in CSD mice (Fig. 3n, o). Next, to investigate the activation of rMR-projecting NE^{LC} neurons under the CRS, *Cre*-dependent retrograde AAV2 carrying recombinase FLP vector was injected into the rMR and the AAV-fDIO-mCherry virus was injected into the LC, which allowed rMR-projecting NE^{LC} neurons to express red fluorescence signals (Supplementary Fig. 7a). The immunostaining results showed that the percentage of TH^{+}/$mCherry^{+}$/c-Fos^{+} neurons among TH^{+}/$mCherry^{+}$ neurons was approximately 55% in CRS mice, which was significantly higher than that in naive mice (Supplementary Fig. 7b, c). The 5-HT^{rMR} neurons were consistently activated by CRS compared to the naive mice (Supplementary Fig. 7d, e).

Collectively, the above results demonstrate that the NE^{LC}-5-HT^{rMR} neural circuit was significantly activated under chronic stress conditions.

Chemogenetic activation of the rMR-projecting NE^{LC} neurons inhibits liver regeneration

To better understand the role of the NE^{LC}-5-HT^{rMR} neural circuit in regulating liver regeneration, we employed chemogenetic manipulations to stimulate this neural circuit. The AAV2/Retro-DIO-FLP virus was stereotaxically injected into the rMR, and the AAV-fDIO-hM3Dq-EGFP or AAV-fDIO-EGFP virus was injected into the LC of *Th-Cre* mice. Three weeks after viral injection, CNO was administered through the drinking water to chronically activate the rMR-projecting NE^{LC} neurons (Fig. 4a). Whole-cell patch-clamp recordings in acute brain slices functionally validated the efficacy of neural activation by showing CNO-induced depolarization of membrane potential of EGFP-positive LC neurons (Fig. 4b, c). Furthermore, c-Fos immunostaining demonstrated the potent activation of rMR-projecting NE^{LC} neurons ($EGFP^{+}$/TH^{+}) (Fig. 4d, e). To assess the regulation of liver regeneration by activating the rMR-projecting NE^{LC} neurons, 70% PHx was performed. We noted that the liver/body weight ratio, as well as the gene and protein expression levels of Ki67 and PCNA, were significantly lower in hM3Dq-EGFP+PHx mice than those of EGFP+PHx mice (Fig. 4f-m). Therefore, chemogenetic activation of the rMR-projecting NE^{LC} neurons could mimic the inhibitory effect of chronic stress on liver regeneration.

Chemogenetic inhibition of the rMR-projecting NE^{LC} neurons reverses the inhibitory effect of chronic stress on liver regeneration

To further study whether the NE^{LC}-5-HT^{rMR} neural circuit is involved in the inhibition of liver regeneration caused by chronic stress, we repressed the activity of the rMR-projecting NE^{LC} neurons. To achieve this goal, we stereotaxically injected a *Cre*-dependent retrograde AAV2 virus carrying a recombinase FLP vector into the rMR, followed by the injection of a *Flp*-dependent recombinant AAV expressing the inhibitory receptor hM4Di, or a control virus (AAV-fDIO-EGFP), into the LC of *Th-Cre* mice (Fig. 5a). Three weeks after the injection, CNO was administered through the drinking water to chronically suppress the rMR-projecting NE^{LC} neurons. Meanwhile, a CSD model was established on both experimental groups. The verification of the chemogenetic inhibition effect was performed through brain slice electrophysiology (Fig. 5b, c) and c-Fos immunostaining (Fig. 5d, e). The results showed that the liver/body weight ratio was significantly higher in hM4Di-EGFP + CSD+PHx mice compared with the EGFP + CSD+PHx mice (Fig. 5f, g). Moreover, both gene and protein expression levels of Ki67 and PCNA were clearly elevated in hM4Di-EGFP + CSD+PHx mice, which almost reached the levels of PHx mice (Fig. 5h-m). Therefore, these data imply that chemogenetic inhibition of the rMR-projecting NE^{LC} neurons could effectively reverse the inhibitory effect of chronic stress on liver regeneration after PHx.

Furthermore, to elucidate the necessity of 5-HT^{rMR} neurons in chronic stress-induced inhibition of liver regeneration, we injected the Cre-dependent recombinant AAV expressing the inhibitory receptor hM4Di, or a control virus (AAV-DIO-mCherry), into the rMR of *Pet1-Cre* mice (Supplementary Fig. 8a). The verification of the chemogenetic inhibition effect was performed through c-Fos immunostaining (Supplementary Fig. 8b, c). The results showed that the protein expression levels of Ki67 and PCNA were significantly elevated in hM4Di-mCherry +CSD+PHx mice, nearly reaching the levels of PHx mice (Supplementary Fig. 8d-g). Therefore, these data imply that chemogenetic

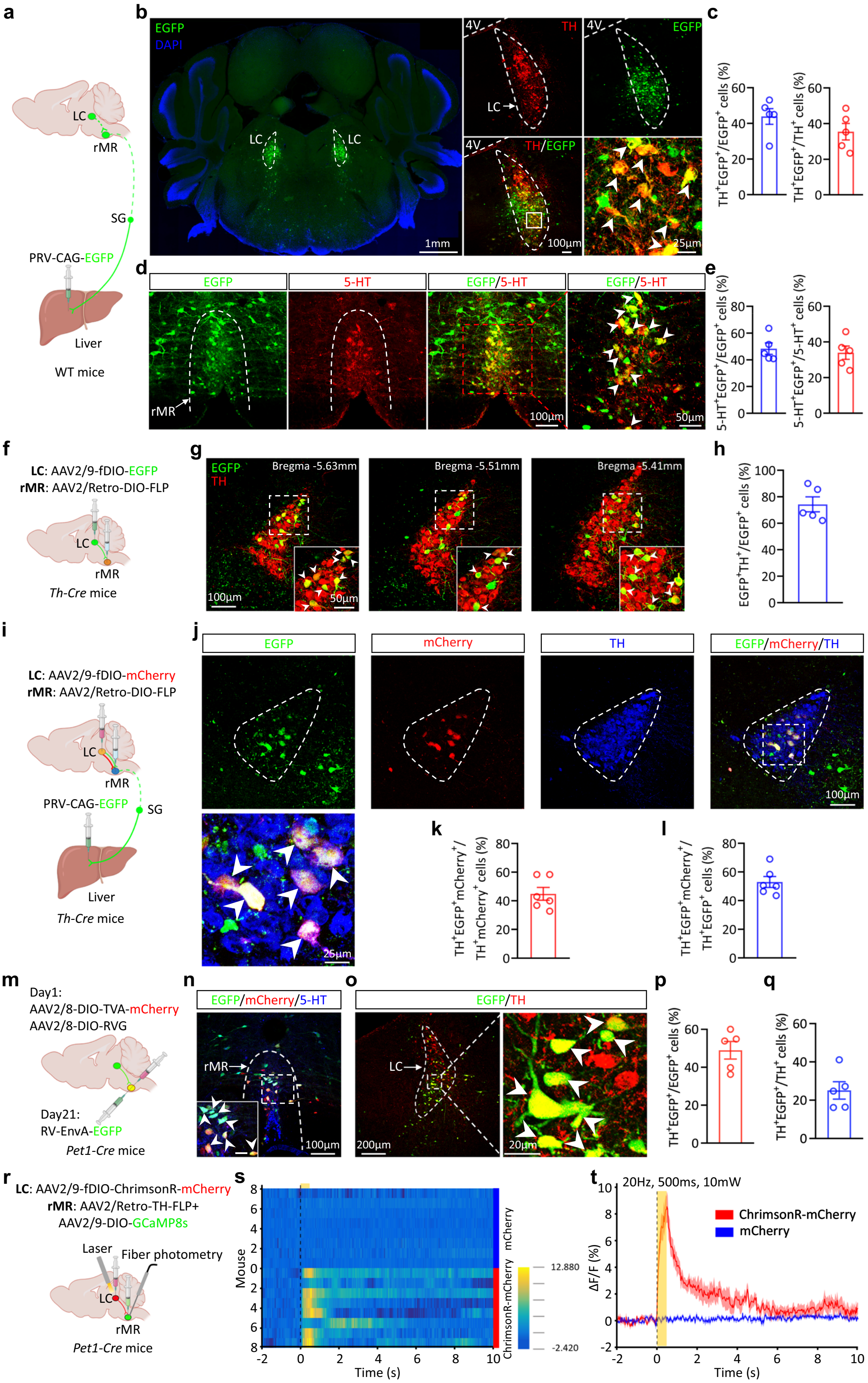

inhibition of the 5-HT^{rMR} neurons could effectively reverse the inhibitory effect of chronic stress on liver regeneration after PHx.

Hepatic sympathetic nerve mediates chronic stress-induced inhibitory effects on liver regeneration

It is widely appreciated that chronic stress activates the sympathetic nervous system (SNS) and causes diverse tissue changes[24]. It has been established that the neural innervations of the liver are predominantly sympathetic[25]. Moreover, hepatic sympathetic nerve activation is linked to the liver regeneration capacity[26]. Therefore, we aimed to investigate whether the hepatic sympathetic nerve plays a crucial role in the inhibition of liver regeneration under chronic stress. During experiments injecting PRV into the liver to trace upstream neural pathways as mentioned previously, it was found that a large number of

Fig. 2 | The NE^{LC}-5-HT^{rMR} neural circuit innervates the liver. **a** Schematic representation of the pseudorabies virus (PRV) injection in the mouse liver for retrograde tracing. Representative images (**b**) and quantification analysis (**c**) showing PRV-labeled neurons colocalized with TH antibody in the LC ($n = 5$ mice). Representative images (**d**) and quantification analysis (**e**) showing PRV-labeled neurons colocalized with 5-HT antibody in the rMR ($n = 5$ mice). Schematic representation of the *Cre*-dependent retrograde AAV tracing strategy (**f**). Representative images of viral expression (green) in the LC of *Th-Cre* mice (**g**) and quantification of co-labeled neurons in EGFP$^+$ neurons (**h**) ($n = 5$ mice). **i** Schematic representation of the *Cre*-dependent retrograde AAV tracing strategy and the PRV injection in the mouse liver. Representative images of PRV expression neurons (green) and rMR-projecting NE^{LC} neurons (red), colocalized with the TH antibody (blue) in the LC of *Th-Cre* mice (**j**) and quantification of co-labeled neurons in TH$^+$/mCherry$^+$ neurons (**k**) and in TH$^+$/EGFP$^+$ neurons (**l**) ($n = 6$ mice). **m** Schematic representation of the *Cre*-dependent and RV-mediated monosynaptic tracing of rMR-projecting LC neurons in *Pet1-Cre* mice. **n** Representative images of viral expression (green with RV and red with TVA) within the rMR neurons and the immunostaining of 5-HT$^+$ neurons (blue) of *Pet1-Cre* mice. Representative images of viral expression (green with RV) within the LC neurons and the immunostaining of TH$^+$ neurons (red) of *Pet1-Cre* mice (**o**) and quantification of co-labeled neurons in TH$^+$ neurons (**p**) and in EGFP$^+$ neurons (**q**) ($n = 5$ mice). **r** Schematic diagram of fiber photometry. Averaged Ca^{2+} heatmaps (**s**) and responses (**t**) evoked by optogenetic activation laser ($n = 8$ mice). Data are represented as mean ± SEM. Source data are provided as a Source Data file. **a, f, i, m** and **r** were created in BioRender. Zhou, Y. (2023) https://BioRender.com/i61q313.

SG neurons were labeled (Supplementary Fig. 9), indicating that the LC-rMR neural circuit traced by PRV may inhibit liver regeneration through the sympathetic nervous system. Next, we further clarified the impact of activating rMR-projecting NE^{LC} neurons on the hepatic sympathetic nervous pathway. Firstly, the AAV2/Retro-DIO-FLP virus was stereotaxically injected into the rMR, and the AAV-fDIO-hM3Dq-mCherry virus was injected into the LC of *Th-Cre* mice. Secondly, the trans-monosynaptic retrograde tracing was conducted by introducing a modified rabies virus (RV-ΔG-EGFP) and helper viruses (AAV2/Retro-RVG-RFP) into the liver parenchyma (Fig. 6a). The immunostaining results demonstrated the effectiveness of virus tracing of liver-projecting SG neurons and rMR-projecting NE^{LC} neurons (Fig. 6b and Supplementary Fig. 10). Importantly, chemogenetic activation of rMR-projecting NE^{LC} neurons could induce significant activation of IML neurons innervating the liver (Fig. 6c, d). These results indicated the functional connection of the LC-rMR-IML-SG-liver pathway.

Furthermore, we detected a higher content of NE in the liver of CSD mice compared with that of naive mice (Fig. 6e, f), indicating the activation of the hepatic sympathetic nerve. In addition, chemogenetic activation of the NE^{LC}-5-HT^{rMR} neural circuit significantly increased the NE content in the liver of naive mice, while chemogenetic inhibition of this projection could markedly reduce the NE content in the liver of CSD mice (Fig. 6g-i).

To further clarify the necessity of sympathetic nerves in chronic stress-induced inhibition of liver regeneration, we performed selective sympathetic denervation (Denerv) of the liver. As previously described[27], a sterile cotton-tipped applicator was soaked in phenol solution (10% phenol in ethyl alcohol) and was carefully applied to the surface of the hepatic artery and portal vein bundles. After 7-day recovery, CSD and 70% PHx were performed consecutively on mice (Fig. 6j). The immunostaining results of both the liver slices and phenol-coated sites showed that hepatic sympathetic nerves were successfully ablated after Denerv (Fig. 6k and Supplementary Fig. 11a). The liver/body weight ratio of Denerv+CSD+PHx mice was significantly higher than that of SH + CSD+PHx mice (Fig. 6l). The protein expression levels of both Ki67 and PCNA were significantly elevated in Denerv +CSD+PHx mice (Fig. 6m-p). In addition, we used the 6-hydroxydopamine (6-OHDA) neurotoxin to induce the chemical denervation of the sympathetic nerve. We found that 6-OHDA treatment could remarkably reduce the NE content in the liver of CSD mice (Fig. 6q, r). Immunofluorescence staining showed that the administration of 6-OHDA almost completely depleted the sympathetic nerve terminals in the liver (Supplementary Fig. 11b). Furthermore, the liver/body weight ratio of 6-OHDA-treated mice without CSD was comparable to that of PHx mice at 48 hours after 70% PHx. Strikingly, 6-OHDA treatment could reverse the decrease in liver/body weight ratio caused by CSD (Fig. 6s). These findings indicate that sympathetic nerve denervation had a positive effect on the restoration of the liver mass. The mRNA and protein expression levels of Ki67 and PCNA corroborated these results (Fig. 6t and Supplementary Fig. 11c-f). These findings suggest that CSD stimulates the SNS, releasing NE from hepatic sympathetic nerve terminals, which will further inhibit liver regeneration.

It is widely known that stressors activate two major pathways, the sympathetic nervous system and the hypothalamic-pituitary-adrenal (HPA) axis[28]. Indeed, the HPA axis dynamically responds to stress via the secretion of endogenous glucocorticoid corticosterone (in rodents) or cortisol (in humans)[27]. To detect how the HPA axis responds in CSD, three key hormones secreted by the adrenal glands were examined. The results showed that compared with naive mice, the levels of adrenaline and corticosterone in CSD mice were significantly increased, and norepinephrine showed an increasing trend, indicating that chronic stress induced activation of the HPA axis (Supplementary Fig. 12a-c). However, we found that adrenalectomy (ADX) or blocking corticosterone biosynthesis in the adrenal gland (using metyrapone) did not affect chronic stress-induced inhibition of liver regeneration (Supplementary Fig. 12d-j and Fig. 13). The above results suggest that the HPA axis is significantly activated under chronic stress, but the activated HPA axis may not mediate the inhibitory effect of chronic stress on liver regeneration.

Chronic stress inhibits liver regeneration by up-regulating the expression of *Adrb2* and inhibiting the polarization of proinflammatory macrophage

To clarify which adrenergic receptor (AR) mediates the effect of NE, we assessed the mRNA expression levels of ARs at 3 hours after 70% PHx under CSD by transcriptome sequencing. The heatmap and qPCR results showed that the expression of adrenergic receptor β2 (*Adrb2*) was significantly increased in CSD+PHx mice compared with PHx mice (Fig. 7a, b and Supplementary Fig. 14). Subsequently, to investigate the role of ADRB2 in CSD induced liver regeneration inhibition, we intraperitoneally applied the ADRB2 specific antagonist ICI 118551 (ICI) to block the function of the ADRB2 receptor (Fig. 7c). *Adrb2* expression was significantly inhibited (Fig. 7d). Notably, the liver/body weight ratio was higher in ICI + CSD+PHx mice than in CSD+PHx mice (Fig. 7e). Additionally, the mRNA expression levels of both *Ki67* and *Pcna* were restored in ICI + CSD+PHx mice (Fig. 7f). The protein expression levels showed similar results (Fig. 7g, h). Furthermore, to clarify the effect of sustained activation of ADRB2 on liver regeneration, we applied the intraperitoneal injection of specific ADRB2 agonist. Formoterol (FORM), a potent, specific, and long-acting adrenergic receptor β2 agonist, was used daily for 21 days (i.e., 1 mg/kg) to sustainedly activate the ADRB2. The results showed that both the liver/body weight ratios, and the mRNA expression levels of *Ki67* and *Pcna* were significantly decreased in FORM+PHx mice compared to Vehicle+PHx mice (Supplementary Fig. 15). Together, these findings suggest that ADRB2 is the major NE receptor mediating the suppression of liver regeneration by chronic stress.

Activation of hepatic macrophages and subsequent release of cytokines are critical steps triggering the initiation of liver regeneration after PHx[29]. Infiltrated macrophages can be divided into two subtypes: alternatively activated reparative macrophages (Ly6C^{lo}),

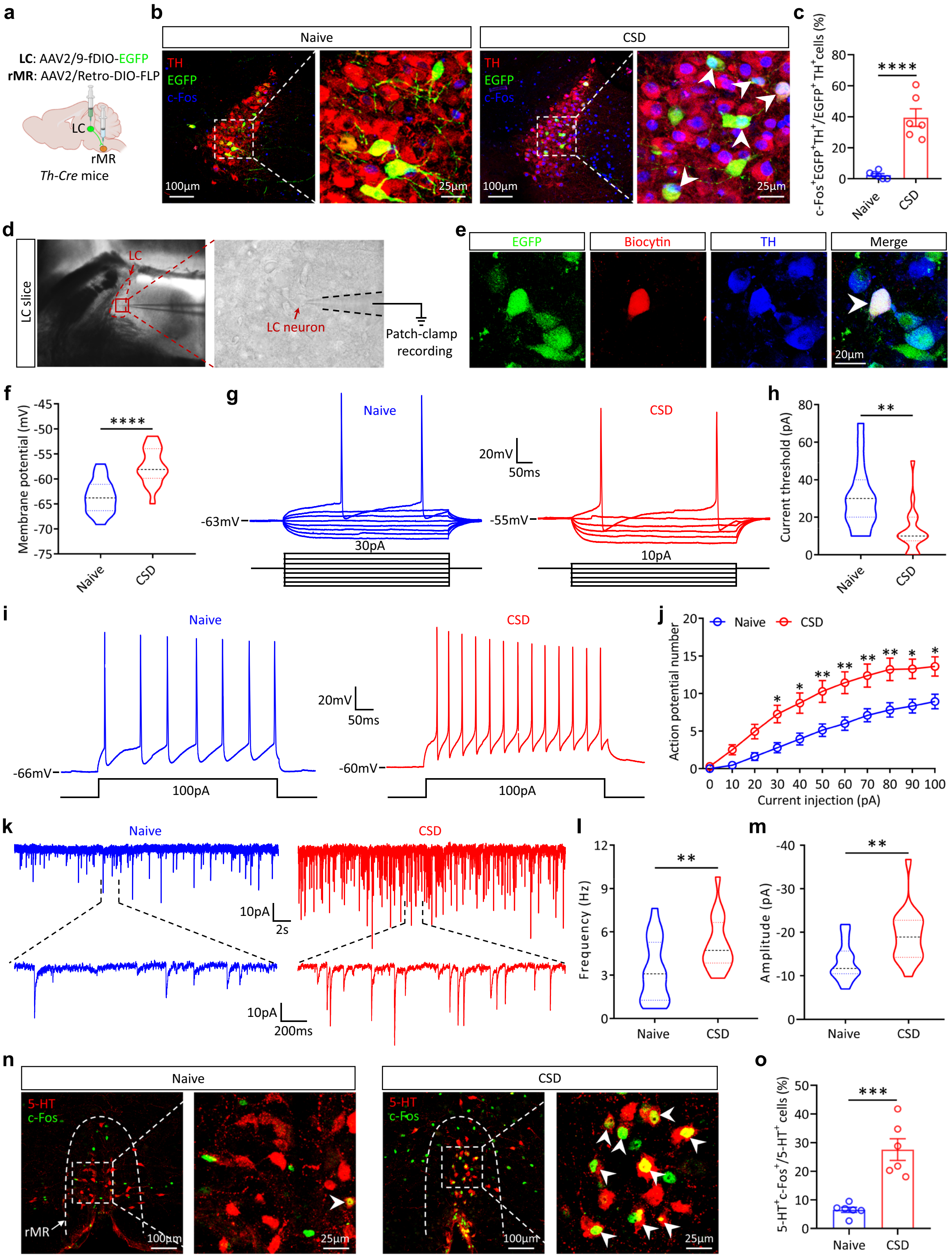

which produce cytokines (such as IL-10, IL-4, and TGF-β1) to reduce inflammation, and classically activated proinflammatory macrophages (Ly6C^{hi}), which release cytokines (such as IL-6, TNF-α, and IL-1β) to increase inflammation[30,31]. Recent research has revealed that Ly6C^{hi} macrophage activation plays an important role in liver regeneration after PHx[32]. Notably, immunofluorescence staining of Raw 264.7 macrophages revealed that ADRB2 had an abundant expression on the macrophage membrane (Supplementary Fig. 16). To explore whether CSD affects liver regeneration by disrupting the initiation process, we analyzed the changes in immune cell composition in the liver at 3 hours after 70% PHx in mice exposed to CSD. Interestingly, flow cytometry analysis revealed no significant difference in the percentages of neutrophils, B cells, and T cells (Supplementary Fig. 17). However, the proportion of hepatic Ly6C^{lo} macrophages was

Fig. 3 | The NE^{LC}-5-HT^{rMR} neural circuit is significantly activated under CSD. **a** Schematic diagram of the *Cre*-dependent retrograde AAV tracing strategy. Representative images of viral expression (green) and c-Fos$^+$ neurons (blue) within TH$^+$ neurons (red) in LC of *Th-Cre* mice (**b**) and the quantification of co-labeled neurons in EGFP$^+$/TH$^+$ neurons in the naive and CSD mice (**c**) ($n = 6$ mice) ****$p < 0.0001$. Representative image of whole-cell recording of one LC neuron (**d**). The rMR-projecting LC neurons (EGFP$^+$) were selected for recording and biocytin was loaded into the cells for post hoc identification of the cell identity (**e**). The experiment was repeated 3 times with similar results. **f** Statistical analysis of resting membrane potential (RMP) in the naive and CSD mice ($n = 18$ cells, from three animals in each group) ****$p < 0.0001$. Representative traces of typical AP responses to a series of 500 ms step current injections recorded from the LC neurons of naive (blue) and CSD (red) mice, respectively (**g**). Statistical analysis of threshold currents in naive and CSD mice (**h**) ($n = 18$ cells, from three animals in each group) **$p = 0.0013$. Representative traces of typical AP response to 100 pA depolarizing current injection recorded from the LC neurons of naive (blue) and CSD (red) mice, respectively (**i**). Statistical analysis of AP number induced by steps current injections (**j**) ($n = 18$ cells, from three animals in each group). For exact p values, see Source Data. Representative traces showing sEPSCs of LC neurons from the naive (blue) and CSD (red) mice, respectively (**k**). Statistical analysis of the average frequency (**l**) and amplitude of sEPSCs (**m**) ($n = 18$ cells, from three animals in each group). (**l**) **$p = 0.0086$, (**m**) **$p = 0.0017$ Representative images of the double immunostaining of 5-HT and c-Fos in the rMR from naive and CSD mice (**n**). The quantification of the co-labeled neurons in 5-HT$^+$ neurons (**o**) ($n = 6$ mice) ***$p = 0.0003$. Two-tailed unpaired t test (**c, f, h, l, m** and **o**); Two-way ANOVA (**j**). Data are represented as mean ± SEM. Source data are provided as a Source Data file. **a** was created in BioRender. Zhou, Y. (2024) https://BioRender.com/u06k157.

significantly higher in CSD+PHx mice compared with PHx mice, while the proportion of Ly6C^{hi} macrophages was significantly lower (Fig. 7i-k). In line with these findings, qPCR analysis showed an increased expression levels of cytokines released by Ly6C^{lo} (*Il-10* and *Il-4*) (Supplementary Fig. 18a) as well as a decreased expression of cytokines pertaining to the Ly6C^{hi} markers (*Il-1β*, *Tnf-α*, and nitric oxide synthase 2 [*Nos2*]) (Supplementary Fig. 18b). ELISA was used to measure the serum expression levels of Ly6C^{hi} markers (IL-6 and TNF-α), revealing similar results to those of the qPCR analysis (Fig. 7l, m). Consistently, we chemogenetically activated the NE^{LC}-5-HT^{rMR} neural circuit in *Th-Cre* mice and discovered that the percentage of hepatic Ly6C^{hi} macrophages was significantly lower in hM3Dq-EGFP+PHx mice compared with EGFP+PHx mice, while the percentage of Ly6C^{lo} macrophages was significantly higher (Fig. 7n-q). Furthermore, we administered ICI as described in the experimental scheme above and then assessed macrophage polarization at 3 hours after PHx. When ADRB2 was inhibited by ICI administration, the proportion of hepatic Ly6C^{hi} macrophages returned to a high level in the CSD mice (Supplementary Fig. 18c-e). Together, these results suggest that CSD could inhibit liver regeneration initiation through interfering with the Ly6C^{lo} to Ly6C^{hi} macrophage polarization. In summary, these data demonstrate that the NE^{LC}-5-HT^{rMR} neural circuit mediates the inhibitory effect of chronic stress on liver regeneration by exciting the hepatic sympathetic nerve/ADRB2/macrophage signaling axis (Fig. 8).

Discussion

This study provides evidence that a “brain-to-liver” signal mediates inhibition of liver regeneration under chronic stress through the hepatic sympathetic nerve/macrophage axis. We have identified a specific neural circuit, NE^{LC}-5-HT^{rMR}, which is responsible for chronic stress-induced inhibition of liver regeneration. Furthermore, the accumulation of NE released by hyperactivated hepatic sympathetic nerves could block proinflammatory macrophage polarization through acting on the ADRB2, which is highly expressed on the macrophage membrane. These findings not only suggest that the NE^{LC}-5-HT^{rMR} neural circuit plays a fundamental role in the homeostasis of liver regeneration, but also provide concepts for precise intervention of chronic stress-evoked liver regeneration capacity impairment in patients with liver disease.

The modern world brings about a high-pressure working environment, leading to increasing numbers of psychological issues, such as anxiety and depression[33,34]. Chronic stress has a profound and broad impact on the physiology of the organism. Sleep deprivation increases food intake in human[35] and rodents[36]. Moreover, the stress induced by sleep fragmentation modulates hematopoiesis[37]. There is substantial evidence indicating that stress would adversely affect the liver function. For example, previous studies have reported that depression caused by chronic stress is linked to metabolic dysfunction-related fatty liver disease, and is also associated with a higher risk of liver disease mortality[38]. Interestingly, our present work showed that a 21-day CSD or CRS exerts a significant inhibitory effect on the liver regeneration capacity (Fig. 1 and Supplementary Fig. 3), which is consistent with the previous findings mentioned above.

Recent years have witnessed an increasing research attention on the peripheral mechanisms underlying liver regeneration. Several signaling pathways, such as Hippo/YAP, Wnt/β-catenin, and NOTCH, have been reported to influence the liver regeneration capacity[39,40]. Yet, the role of the central nervous system in liver regeneration remains to be delineated. Persistent stress causes different parts of the brain to react through the neuroendocrine pathways and the autonomic nervous system[41,42]. Indeed, it has been shown that long-term stress could lead to structural and functional alterations in many brain regions, which could subsequently cause dysfunctions in peripheral organs[43]. However, the brain regions or circuits that innervate the liver and respond to chronic stress have yet to be identified. In this context, the current study revealed NE neurons in the LC and 5-HT neurons in the rMR as one of the most critical substrates for liver regeneration. It is noteworthy that the LC-NE system is a fundamental component of the stress system. Additionally, 5-HT neurons in the rMR, which activates the SNS as premotor neurons[20], are stimulated during chronic stress. Strikingly, we demonstrated a structural and functional connection from NE^{LC} neurons to 5-HT^{rMR} neurons, which were dramatically activated during chronic stress (Figs. 2, 3). Importantly, chemogenetic activation of the NE^{LC}-rMR circuit mimics the chronic stress-induced impairment on liver regeneration, while chemogenetic silencing of the same circuit could reverse chronic stress-induced liver regeneration deficits (Figs. 4, 5). Thus, the LC-rMR neural circuit can be considered as a vital component of the neural pathways innervating the liver and regulating the capacity of liver regeneration.

The SNS is one of the most important components that mediate stress responses. For many years, the autonomic innervation of liver tissue has been discussed[44], but a lack of advanced tracing and imaging approaches has greatly limited our full understanding of this process. Excitingly, with the use of 3D imaging, recent studies have clearly demonstrated that both human and mouse livers were densely innervated by sympathetic nerves[25]. We discovered that the NE content in the liver was significantly increased after chronic stress, indicating the hyperactivation of hepatic sympathetic nerves (Fig. 6a, b). Nevertheless, the role of hepatic sympathetic nerves in liver regeneration is still being debated. Some studies have suggested that hepatic sympathectomy does not affect liver regeneration[45,46]. By contrast, other studies have argued that the NE neurotransmitter, released by sympathetic nerves, would promote the proliferation of hepatocyte via augmenting the epidermal growth factor (EGF) effects[47]. However, there is also evidence indicating that inhibition of the SNS could reduce liver damage by increasing the accumulation of hepatic progenitor cells[48]. Here, we have contributed the findings that chronic stress leads to the hyperactivation of SNS through the NE^{LC}-5-HT^{rMR} neural circuit, and subsequent accumulation of NE could impede liver regeneration. However, such effect could be reversed by hepatic

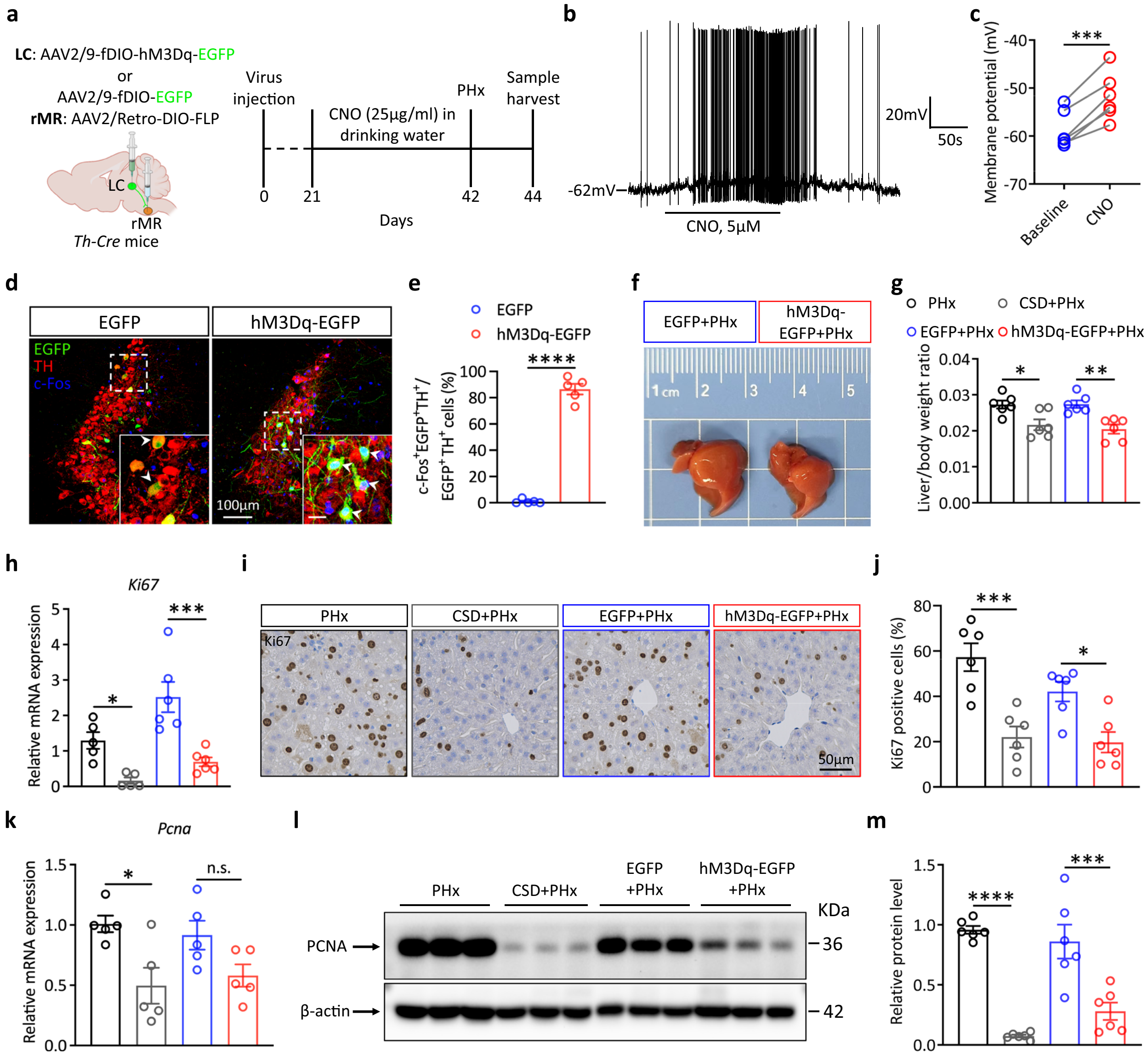

Fig. 4 | Chemogenetic activation of the rMR-projecting NE^{LC} neurons impairs liver regeneration. a Schematic representation of the viral strategy for chemogenetic manipulation of the rMR-projecting NE^{LC} neurons and the timeline of the experiments. Brain slice electrophysiology showing that CNO caused a rapid depolarization of EGFP$^+$ LC neurons in hM3Dq-EGFP mice (**b**). The quantification of membrane potential changes (**c**) ($n = 6$ cells from 3 mice) $^{***}p = 0.0006$. Representative images of LC immunostaining with c-Fos and TH antibodies in EGFP and hM3Dq-EGFP mice after a three-week CNO intake (**d**) and quantification of c-Fos$^+$/EGFP$^+$/TH$^+$ neurons in EGFP$^+$/TH$^+$ neurons (**e**) ($n = 5$ mice) $^{****}p < 0.0001$. Scale bar, 20 μm. **f** Representative liver tissue images collected at 48 hours after 70% PHx in EGFP and hM3Dq-EGFP mice. **g** The liver/body weight ratio of PHx, CSD+PHx, EGFP+PHx, and hM3Dq-EGFP+PHx mice ($n = 6$ mice) $^*p = 0.0219$, $^{**}p = 0.0041$. **h** The mRNA expression levels of *Ki67* at 48 hours after 70% PHx for each group of mice ($n = 5$, 5, 6 and 6 mice, respectively) $^*p = 0.0498$, $^{***}p = 0.0005$. Representative photographs showing the immunohistochemical staining of Ki67 at 48 hours after 70% PHx (**i**) and quantification of Ki67-positive cells (**j**) ($n = 6$ mice) $^{***}p = 0.0004$, $^*p = 0.0217$. **k** The mRNA expression levels of *Pcna* at 48 hours after 70% PHx for each group of mice ($n = 5$mice) $^*p = 0.0238$, n.s. $p = 0.1898$. Representative western blot images showing the expression of PCNA protein in liver tissue (**l**) and quantification data (**m**) ($n = 6$ mice) $^{****}p < 0.0001$, $^{***}p = 0.0003$. Two-tailed *paired t* test (**c**); two-tailed unpaired *t* test (**e**); one-way ANOVA (**g, h, j, k** and **m**). Data are represented as mean ± SEM. Source data are provided as a Source Data file. **a** was created in BioRender. Zhou, Y. (2024) https://BioRender.com/u06k157.

sympathetic denervation (Fig. 6 and Supplementary Fig. 11). Consistently, chronic hepatic sympathetic overactivation has been reported to promote the hepatic steatosis[27]. Notably, another important pathway that responds to stress, the HPA axis, was also found to be significantly activated in CSD. However, our evidence suggests that the activated HPA axis may not mediate the inhibitory effect of chronic stress on liver regeneration.

The neurotransmitter NE maintains the balance of multiple hepatic functions through specific binding to particular AR. ARs are mainly composed of α-ARs and β-ARs[49]. The α-ARs, which are highly expressed in hepatocytes, have been reported to promote DNA synthesis by binding with NE[50]. However, activation of ADRB2 reduces the release of TNF-α from hepatic macrophages[51], which may inhibit the activation of proinflammatory macrophages. Here, we demonstrate that *Adrb2* mRNA expression levels were substantially elevated among numerous ARs at 3 hours after PHx in CSD mice, and ADRB2 was present on the macrophage membrane (Fig. 7 and Supplementary Figs. 14, 16). As such, it is conceivable that chronic stress drives a substantial increase in the content of NE in the liver. After PHx, released NE binds to ADRB2, thereby inhibiting the liver regeneration. Thus, both our findings and previous studies suggest that different activation levels of distinct subtypes of ARs may produce complex

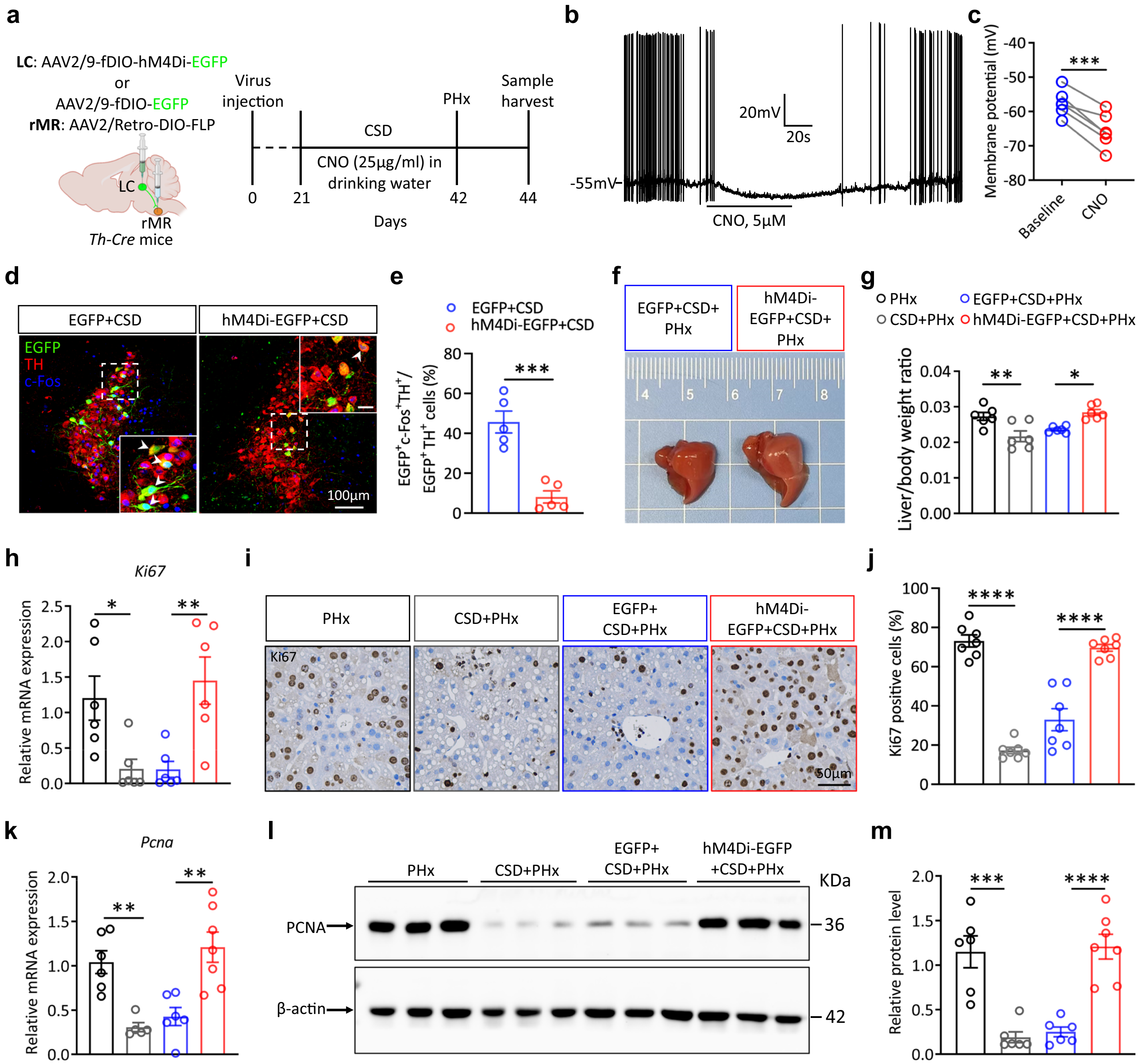

Fig. 5 | Chemogenetic inhibition of rMR-projecting NE^{LC} neurons reverses the inhibitory effects of chronic stress on liver regeneration. a Schematic representation of the viral strategy for chemogenetic manipulation of the NE^{LC}-rMR projection and the timeline of the experiments. Brain slice electrophysiology showing that CNO caused a rapid hyperpolarization of EGFP$^+$ LC neurons in hM4Di-EGFP + CSD mice (**b**). The quantification of membrane potential changes was shown in (**c**) ($n = 6$ cells from 3 mice) $^{***}p = 0.0006$. Representative images of LC immunostaining with c-Fos and TH antibodies in EGFP + CSD and hM4Di-EGFP + CSD mice after CSD (**d**) and quantification of c-Fos$^+$/EGFP$^+$/TH$^+$ neurons in EGFP$^+$/TH$^+$ neurons (**e**) ($n = 5$ mice) $^{***}p = 0.0003$. Scale bar, 20μm. **f** Representative liver tissue images collected at 48 hours after 70% PHx in EGFP + CSD+PHx and hM4Di-EGFP + CSD+PHx mice. **g** The liver/body weight ratio of mice in PHx, CSD+PHx, EGFP + CSD+PHx and hM4Di-EGFP + CSD+PHx groups ($n = 6$ mice) $^{**}p = 0.0055$, $^{*}p = 0.0163$. **h** The mRNA expression levels of *Ki67* at 48 hours after 70% PHx for each group of mice ($n = 6$ mice) $^{*}p = 0.0416$, $^{**}p = 0.0085$. Representative photographs showing the immunohistochemical staining of Ki67 at 48 hours after 70% PHx (**i**) and quantification of Ki67-positive cells (**j**) ($n = 7$ mice) $^{****}p < 0.0001$. **k** The mRNA expression levels of *Pcna* at 48 hours after 70% PHx for each group of mice ($n = 6$, 5, 6 and 7 mice, respectively) $^{**}p = 0.0063$, $^{**}p = 0.0016$. Representative western blot images showing the expression of PCNA protein in liver tissue (**l**) and quantification data (**m**) ($n = 6$, 6, 6 and 7 mice, respectively) $^{***}p = 0.0001$, $^{****}p < 0.0001$. Two-tailed paired *t* test (**c**); two-tailed unpaired *t* test (**e**); one-way ANOVA (**g**, **h**, **j**, **k** and **m**). Data are represented as mean ± SEM. Source data are provided as a Source Data file. a was created in BioRender. Zhou, Y. (2024) https://BioRender.com/u06k157.

even contrasting effects on the liver function, which still needs further exploration.

Physically, hepatocytes are typically in a quiescent state (the G_0 phase of the cell cycle). However, stressors like PHx can prime the cell proliferative process, which is largely dependent on interactions between hepatocytes and non-parenchymal cells[52]. The polarization status of macrophages during this priming phase is the trigger of entering into the cell cycle (G_0 to G_1 transition) and hence hepatocyte proliferation[53]. Cytokines released by Ly6C^{hi} macrophages, such as IL-6 and TNF-α, are essential for liver regeneration after PHx. IL-6 is a major driver of hepatocyte proliferation, with its expression levels increased by TNF-α shortly after PHx[54]. In this study, it was demonstrated that CSD blocked the proinflammatory macrophage polarization by activating the NE^{LC}-5-HT^{rMR} neural circuit, which suppressed the production of IL-6 and TNF-α, subsequently inhibiting liver regeneration in the initiation phase.

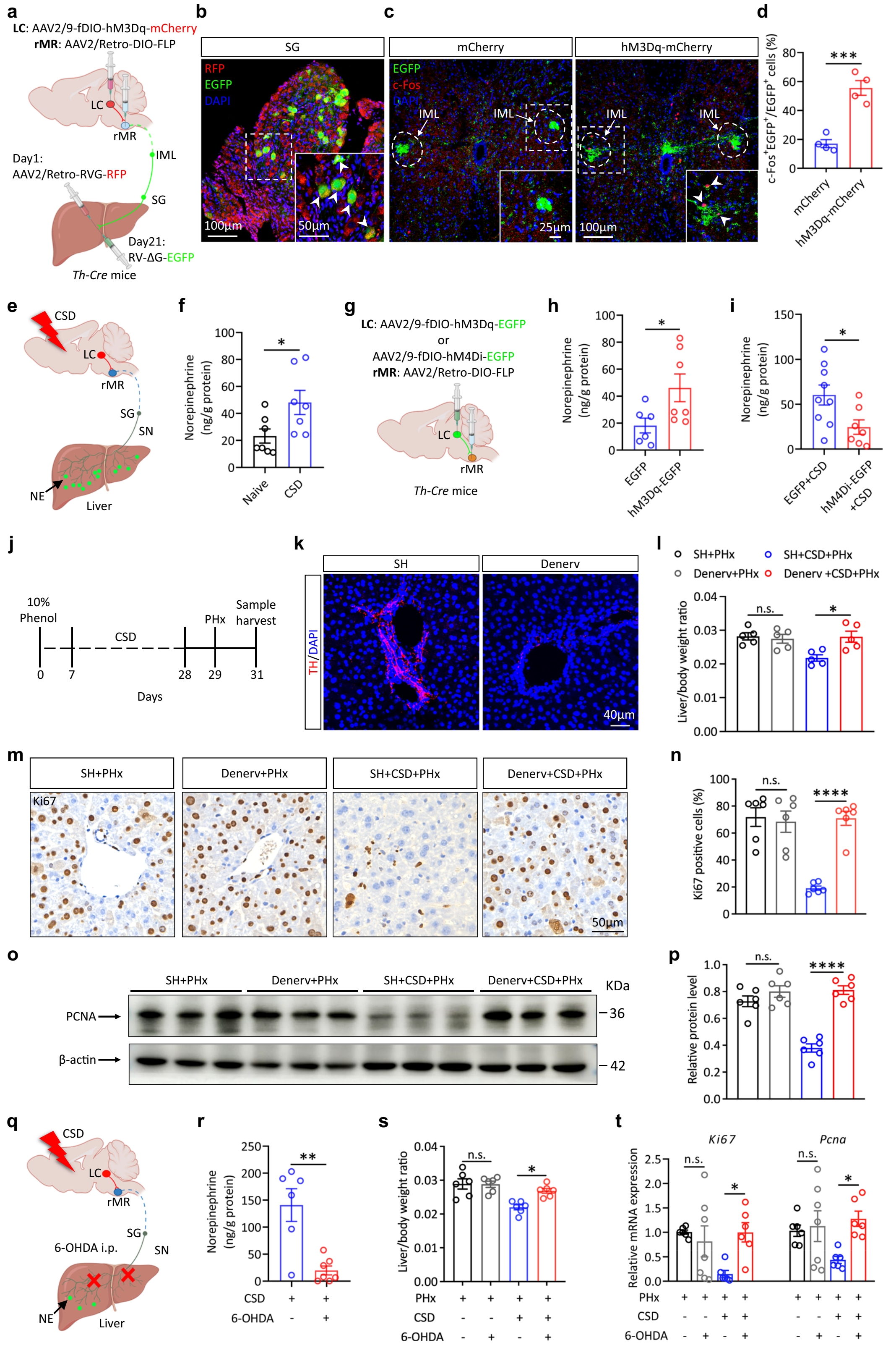

In summary, the present study uncovers a “brain-to-liver” signal that is implicated in the negative impact of chronic stress on liver regeneration. These results add a dimension into brain control of peripheral visceral organs. Moreover, the NE^{LC}-5-HT^{rMR}-hepatic sympathetic nerve-macrophage axis might emerge as a potential therapeutic target to improve liver regeneration and promote functional recovery in patients undergoing liver surgery or with severe liver injuries.

Methods

Animals

Adult male *Th-Cre* mice were obtained from the Professor Wei L Shen’s Laboratory (School of Life Science and Technology, ShanghaiTech University). Adult male *Pet1-Cre* mice were purchased from the Jackson Laboratory. Adult male wild type (WT) C57BL/6 mice were purchased from Shanghai Jiesijie Laboratory Animal Co., Ltd. All animals were

Fig. 6 | Hepatic sympathetic denervation reverses inhibitory effects of chronic stress on liver regeneration. a Schematic representation of the viral strategy for chemogenetic manipulation of the NE^{LC}-rMR projection and RV-mediated monosynaptic tracing in liver-projecting SG neurons. **b** Representative images of viral expression within SG neurons. The experiment was repeated 3 times with similar results. Representative images of viral expression within the IML neurons and immunostaining of c-Fos^{+} neurons (**c**) and quantification of co-labeled neurons (**d**) ($n = 4$) $^{***}p = 0.0006$. Schematic representation of NE release from the hepatic sympathetic nerve after chronic stress (**e**) and the increased content of NE in the liver (**f**) ($n = 7$) $^{*}p = 0.0337$. **g** Schematic representation of the viral strategy for chemogenetic manipulation. **h** The NE content in the liver after chemogenetic activation of the rMR-projecting NE^{LC} neurons ($n = 6$ and 7) $^{*}p = 0.0433$. **i** The NE content in the liver of mice after chemogenetic inhibition of rMR-projecting NE^{LC} neurons ($n = 9$ and 7) $^{*}p = 0.0274$. **j** Timeline of the selective sympathetic denervation experiments. **k** Immunostaining images of TH in liver slices in SH and Denerv mice. **l** Liver/body weight ratio in four groups ($n = 5$) n.s. $p = 0.9777$, $^{*}p = 0.0140$. Representative photographs showing the immunohistochemical staining of Ki67 (**m**) and quantification data (**n**) ($n = 6$) n.s. $p = 0.9990$, $^{****}p < 0.0001$. Representative western blot images showing the expression of PCNA protein in liver tissue (**o**) and quantification data (**p**) ($n = 6$) n.s. $p = 0.5161$, $^{****}p < 0.0001$. Schematic representation of the hepatic sympathetic denervation by 6-OHDA (**q**) and reduces the NE content in the liver of CSD mice (**r**) ($n = 6$ and 7, respectively) $^{**}p = 0.0016$. **s** Liver/body weight ratio in four groups ($n = 6$) n.s. $p = 0.9999$, $^{*}p = 0.015$. **t** Gene expression levels of *Ki67* and *Pcna* in the four groups ($n = 6$, 7, 6 and 6) (left: n.s. $p = 0.9101$, $^{*}p = 0.0428$; right: n.s. $p = 0.9869$, $^{*}p = 0.0428$). One-way ANOVA (**l, n, p, s** and **t**); two-tailed unpaired *t* test (**d, f, h, i** and **r**); No adjustment is made for multiple comparisons in **f**, **h**, and **i**. Data are represented as mean ± SEM. Source data are provided as a Source Data file. **a, e, g** and **q** were created in BioRender. Zhou, Y. (2024) https://BioRender.com/f77e322.

housed in a temperature-controlled room (22-25°C) with a 12 h light/dark cycle, and food plus water available ad libitum. Mice were randomly assigned to experimental groups. The investigator was blinded to group identity during the experiment and quantitative analyses. All animal procedures were approved by the Ethics Committee for Experimental Use of Animals of Shanghai Jiao Tong University School of Medicine (SYXK-2013-0050).

Cell culture

The Raw 264.7 cell line was obtained from Procell Life Science & Technology Co.,Ltd. The cell line was cultured in DMEM medium (Thermo Fisher Scientific) supplemented with 10% fetal bovine serum (Thermo Fisher Scientific) at 37°C in a 5% CO_2 humidified incubator.

Chronic stress model construction

Chronic sleep deprivation (CSD) and chronic restraint stress (CRS) are considered chronic stress models in mice that simulate the clinical stressful state like sleep loss and anxiety[55,56].

Restraint stress was carried out as described previously[57]. Briefly, the mice were placed in ventilated 50 ml conical tubes for 2 hours started randomly each day. Holes were drilled on the tubes so that mice could breathe freely. For CRS model, the stress procedure maintained for 21 days.

Sleep deprivation procedure was constructed as described previously[58]. Sleep deprivation began from 9 AM to 5 PM in a multiple platform water bath. Twelve small platforms were placed in a water tank and eight mice were placed in a same water bath. Every mouse could move between platforms and obtain water and food during the procedure. The water tank was filled water and the height was 1 cm lower than the platform. When mice fell asleep, muscle atonia would cause them to fall into water. Throughout the experiments, clean water was replaced every day. For CSD model, the stress procedure maintained for 21 days.

Partial hepatectomy (PHx) model

Male WT or *Th-Cre* mice (8-10 weeks old) were subjected to 70% or 90% PHx as described previously[59,60]. Briefly, mice were kept anesthetized by isoflurane and a midline abdominal skin and muscle incision were made to expose the liver. As for the 70% PHx model, the median and left lateral lobes were removed respectively after pedicle ligation. For the 90% PHx model, the right lateral lobe was to be additionally removed. Thereafter, the ventral incision was sequentially closed. Mice were sacrificed at 3, 12, 24, 48, and 72 hours after PHx by cervical dislocation. Liver samples and serum samples were collected for examination.

Adrenalectomy (ADX)

Male WT mice were kept anesthetized by isoflurane and small incisions were made on the back skin above bilateral adrenal gland. Both adrenal glands were carefully removed with a pair of curved forceps. Sham mice were performed the same procedures as the ADX mice, except for the removal of adrenal glands. Drinking water was supplemented with 0.9% saline solution for both ADX and sham mice.

Phenol-based hepatic sympathetic nerve denervation

Male WT mice were kept anesthetized by isoflurane and a midline abdominal skin and muscle incision were made to expose the hepatic artery, portal vein and common bile duct. For denervation of the hepatic sympathetic nerves (Denerv), a sterile cotton-tipped applicator was soaked in phenol solution (10% phenol in ethyl alcohol) and carefully applied to the surface of the bundle of the hepatic artery and portal vein. The abdominal cavity was washed using 0.9% saline solution to minimize the adhesion formation. The sham mice were performed the same procedures as the Denerv mice, except that the solution applied was 0.9% saline.

Anxiety-like behavior test

For the open field test (OFT), the open filed chamber was made of white plastic (40 cm×40 cm×40 cm) and a 20 cm×20 cm center square was defined as the central area. Mice were placed into the center individually and their spontaneous behavior was monitored for 10 minutes. The time spent in center and total distance were recorded and analyzed throughout the experiment. The chamber was cleaned with 75% ethanol after each trial.

For the elevated plus maze (EPM) test, the maze apparatus consisted of two opposing open (40 cm × 5 cm) and two enclosed (40 cm × 5 cm) arms extending from a central platform (5 cm×5 cm). The apparatus was raised 40 cm above the floor. Mice were placed into the center square of the maze individually and their spontaneous behavior was monitored for 5 minutes. The total distance and the time they spent in the open arms were recorded and analyzed throughout the experiment. The apparatus was cleaned with 75% ethanol after each trial.

Liver immunohistochemistry (IHC) staining

Liver samples were fixed in 4% formaldehyde for at least 24 hours, embedded in paraffin, and then cut into 4-µm-thick sections. Liver sections were deparaffinized using xylene, rehydrated with graded ethanol, and incubated with 3% hydrogen peroxide. After antigen retrieval, the sections were blocked with 10% normal goat serum and were then incubated in primary antibodies overnight at 4 °C (Ki67 1:500, GB111141, Servicebio). The next day, sections were washed 3 times with PBS, then incubated in secondary antibody for 1 hour.

Quantitative polymerase chain reaction (qPCR)

Total RNA was isolated from liver tissue from different experimental mice using the Tissue RNA purification Kit (EZBioscience, China). The purified RNA was reverse transcribed into cDNA using 4× EZscript Reverse

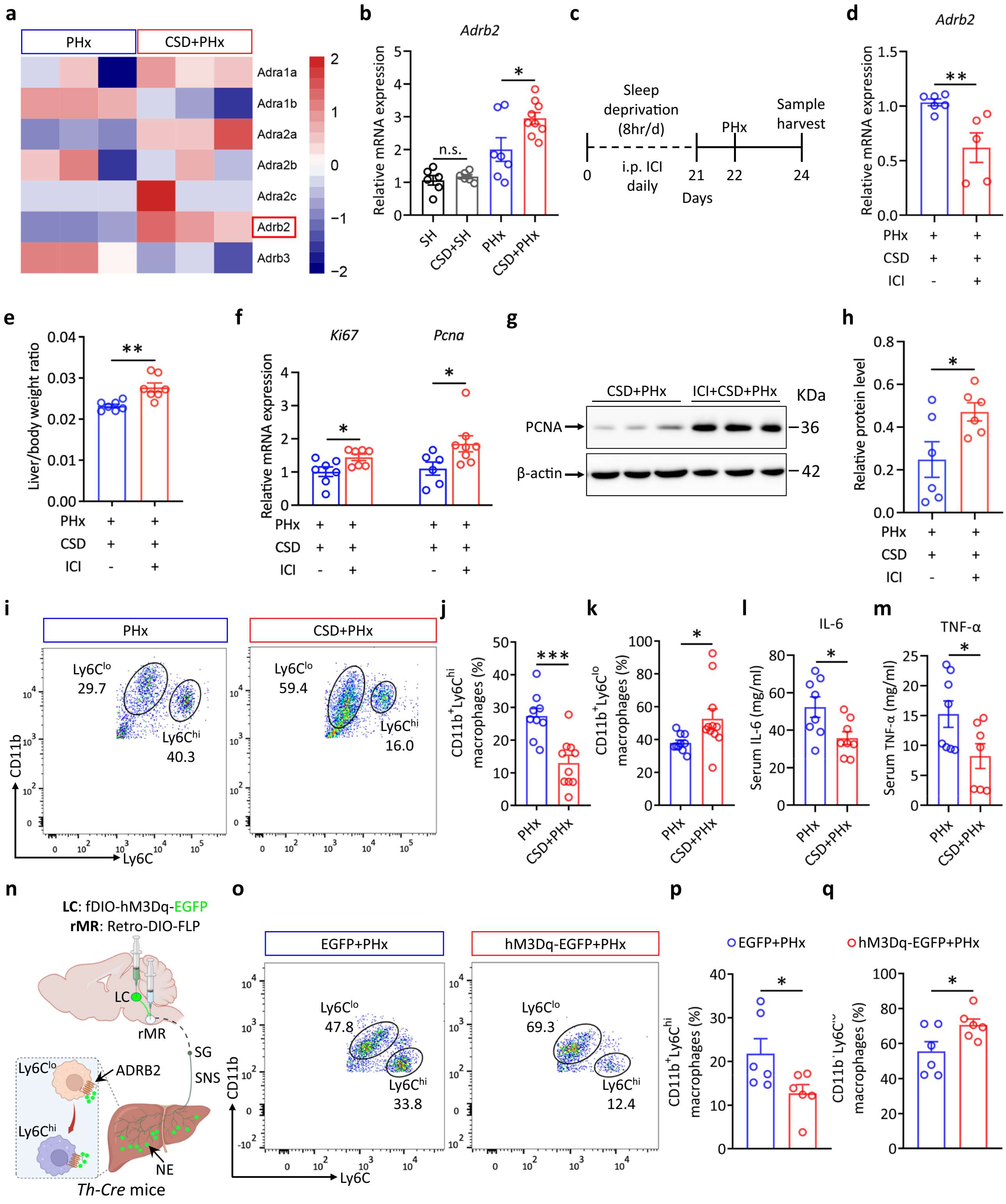

Transcription Mix II for qPCR (EZBioscience, China). All procedures were operated according to the manufacturer's protocol. Quantitative real-time PCR was performed using a real-time PCR system with 2×SYBR Green qPCR Master Mix (EZBioscience, China). GAPDH was used as internal control. The primer sequences are listed in Supplementary Table 1.

Western blotting

Liver tissues were subjected to Western blotting analysis as described previously[54]. The liver tissues collected from different experimental mice were lysed in RIPA lysis buffer (P0013B, Beyotime, China) containing the phosphatase inhibitor and protease inhibitor (P1045, Beyotime, China). The total proteins were extracted by centrifugation (12000 g, 15 min). The quantification of the protein concentration was accomplished with a BCA kit (23225, Thermo, USA). The equal-quality protein samples were separated by 10% SDS-PAGE, transferred to PVDF membranes and blocked with the 5% bovine serum protein (BSA) solution, immunoblotted with the indicated primary antibodies overnight at 4°C and then incubated with

Fig. 7 | Chronic stress inhibits liver regeneration by up-regulating the expression of *Adrb2* and inhibiting the polarization of proinflammatory macrophages. RNA-seq analysis of liver tissue from PHx and CSD+PHx mice, 3 hours after 70% PHx ($n = 3$ mice). The heatmap shows the AR gene expression level profiles in the two groups (**a**). AR, adrenergic receptors. mRNA expression levels of *Adrb2* show a significant increase in CSD+PHx mice (**b**), 3 hours after 70% PHx ($n = 6$, 6, 7 and 9 mice, respectively). n.s. $p = 0.9875$, $^{*}p = 0.0198$. **c** The timeline of vehicle or ICI administration in daily CSD experiments. **d** The mRNA expression levels of *Adrb2* in liver were significantly decreased after ICI administration in ICI + CSD+PHx mice ($n = 6$ and 5 mice, respectively). $^{**}p = 0.0098$. **e** Liver/body weight ratio of vehicle +CSD+PHx and ICI + CSD+PHx mice at 48 hours after 70% PHx ($n = 7$ mice). $^{**}p = 0.0024$. **f** mRNA expression levels of *Ki67* (left, $n = 7$ mice, $^{*}p = 0.0413$) and *Pcna* (right, $n = 6$ and 8 mice, respectively, $^{*}p = 0.0269$) in the two groups. Representative western blot images showing the expression of PCNA protein in liver tissue (**g**) and quantification data (**h**) ($n = 6$ mice). $^{*}p = 0.0381$. Representative FACS plots (**i**) and quantifications of Ly6C^{hi} (**j**) ($n = 9$ and 10 mice, respectively, $^{***}p = 0.0004$) and Ly6C^{lo} (**k**) ($n = 10$ and 11 mice, respectively, $^{*}p = 0.0352$) hepatic macrophages at 3 hours after PHx in PHx and CSD+PHx mice. ELISA analysis of serum IL-6 (**l**) ($n = 8$ mice, $^{*}p = 0.0226$) and TNF-α (**m**) ($n = 8$ and 7 mice, respectively $^{*}p = 0.0393$) levels in PHx and CSD+PHx mice ($n = 7$-8 mice). **n** Schematic representation of the detection of hepatic macrophages after chemogenetic activation of the NE^{LC}-5-HT^{rMR} neural circuit. Representative FACS plots (**o**) and quantifications of Ly6C^{hi} (**p**) and Ly6C^{lo} (**q**) hepatic macrophages at 3 hours after PHx in EGFP+PHx and hM3Dq-EGFP+PHx mice ($n = 6$ mice) (**p**) $^{*}p = 0.0461$, (**q**) $^{*}p = 0.0419$. One-way ANOVA (**b**); two-tailed unpaired t test (**d**, **e**, **f**, **h**, **j**, **k**, **l**, **m**, **p** and **q**); n.s., not significant; Data are represented as mean ± SEM. Source data are provided as a Source Data file. n was created in BioRender. Zhou, Y. (2024) https://BioRender.com/u03v312.

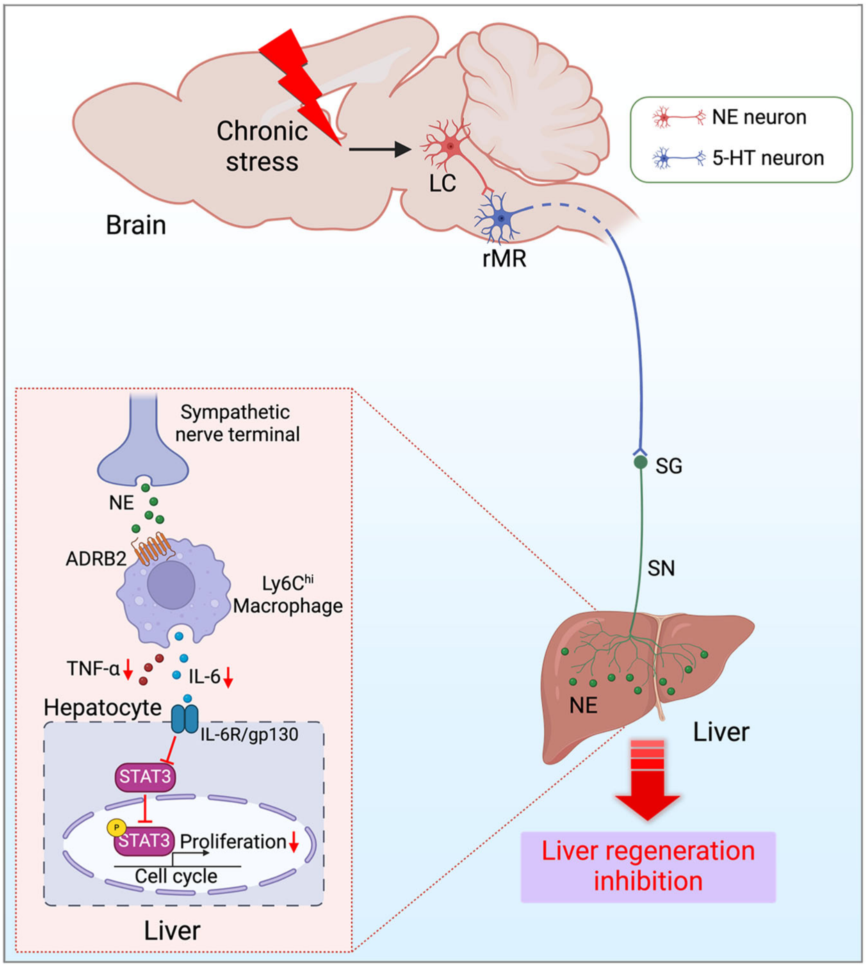

Fig. 8 | Summary of brain-to-liver axis mediating the inhibition of liver regeneration under chronic stress. Chronic stress activates the NE^{LC}-5-HT^{rMR} neural circuit, which downstream drives a continuous release of NE from the hepatic sympathetic nerve terminals. Accumulated NE can block the polarization of proinflammatory macrophages by acting on ADRB2, subsequently inhibiting liver regeneration in the initiation phase. Created in BioRender. Zhou, Y. (2022) https://BioRender.com/v10p106.

the corresponding HRP-coupled secondary antibodies. Finally, the signals were visualized with ECL buffer kit (E411-04, Vazyme, China) and the signals were detected with .... The primary antibodies are listed as follows: PCNA (1:1000, ab29, Abcam), β-actin (1:10000, 66009-1-Ig, Proteintech, USA) and the secondary antibody is the HRP-conjugated Affinipure Goat Anti-Mouse IgG (SA00001-1, Proteintech, USA).

Pseudorabies virus (PRV) injection

Briefly, under anesthesia, WT mice were exposed, and 5 injections (1 µl per site) were made into the liver parenchyma. Each site was injected over 5 minutes and the needle was left in place for 5 additional minutes. The mice were perfused at the time point when symptoms of infection appeared, usually between the 6th and 7th days post-injection. PRV-CAG-EGFP was purchased from BrainVTA (China).

Viral injections

Mice were anesthetized with sodium pentobarbital (50 mg/kg, i.p.) and secured in a stereotactic frame (RWD Instruments). A midline scalp incision was made and a hole was drilled on the skull to allow the passage of glass pipette filled with the virus. Thereafter, the virus was injected into LC (coordinates from Bregma: AP: -5.45 mm, ML: ±1.00 mm, DV: -3.80 mm) and rMR (coordinates from Bregma: AP: −5.90 mm, ML: 0 mm, DV: −5.75 mm) at a speed of 40 nl/min, allowing an additional 10 minutes for viral particles to diffuse before pipette was slowly withdrawn. The viruses, including, AAV2/9-EF1α-fDIO-EGFP-WPRE-hGH-pA, AAV2/retro-EF1α-DIO-FLP-WPRE-hGH-pA, AAV2/9-EF1α-fDIO-hM3D(Gq)-EGFP-WPRE-hGH-pA, AAV2/9-EF1α-fDIO-hM4D(Gi)-EGFP-WPRE-hGH-pA, AAV2/1-hSyn-CRE-WPRE-hGH-pA and AAV2/9-EF1a-DIO-mCherry-WPRE-hGH-pA, was purchased from BrainVTA (China).

Immunofluorescence (IF) staining

Brain samples were fixed in 4% formaldehyde for at least 6 hours, dehydrated by 30% sucrose and then cut into 30-μm-thick sections. The antigens were retrieved by incubation overnight at 4°C with the following primary antibodies: 5-HT (1:1000, GT20079, Neuromics), TH (1:1000, ab134461, Abcam), c-Fos (1:1000, ab190289, Abcam), ADRB2 (1:100, ab182136, Abcam), GPER (1:1000, LS-A4272, LSBio) and tdTomato (1:800, EST203, Kerafast). The sections were then incubated with fluorescence conjugated secondary antibodies (1:1000, Abcam) at room temperature for 1.5 hours. The secondary antibodies used in this study were as follows: Goat anti-Chicken IgY H&L (Alexa Fluor 405, ab175674), Donkey anti-Goat IgG H&L (Alexa Fluor 405, ab175664), Goat anti-Chicken IgY H&L (Alexa Fluor 488, ab150169), Donkey anti-Goat IgG H&L (Alexa Fluor 488, ab150129), Donkey anti-Goat IgG H&L (Alexa Fluor 594, ab150136), Goat anti-Chicken IgY H&L (Alexa Fluor 594, ab150176) and Donkey anti-Rat IgG H&L (Alexa Fluor 594, Ab150156).

Brain slice electrophysiology

Brain slice preparation. Mice were deeply anesthetized with pentobarbital sodium (0.5% w/v, i.p.) and intracardially perfused with ~20 ml oxygenated modified NMDG artificial cerebrospinal fluid (NMDG ACSF) that contained (in mM) 92 N-methyl-d-glucamine (NMDG), 2.5 KCl, 1.25 NaH_2PO_4, 30 $NaHCO_3$, 20 HEPES, 25 Glucose, 2 Thiourea, 5 Na-ascorbate, 3 Na-pyruvate, 0.5 $CaCl_2$ and 10 $MgSO_4$. The pH of NMDG ACSF was adjusted to 7.3 with concentrated HCl and the osmolarity was 300–305 mOsm. Coronal slices (200 μm) that contained the LC were sectioned at 0.14 mm/s on a vibrating microtome (VT1200s, Leica). The brain slices were initially incubated in NMDG ACSF for 10–12 minutes at 33 °C, followed by HEPES ACSF that contained (in mM) 92 NaCl, 2.5 KCl, 1.25 NaH_2PO_4, 30 $NaHCO_3$, 20 HEPES, 25 Glucose, 2 Thiourea, 5 Na-ascorbate, 3 Na-pyruvate, 2 $CaCl_2$ and 2 $MgSO_4$ (pH 7.3–7.4) for at least 1 hour at 25 °C. Then, the brain slices were transferred to a slice chamber (Warner Instruments) for electrophysiological recording and were continuously perfused with standard ACSF that contained (in mM) 125 NaCl, 2 $CaCl_2$, 2.5 KCl, 1 $MgCl_2$, 25 $NaHCO_3$, 1.25 NaH_2PO_4 and 12.5 glucose (pH 7.3–7.4) at 2.5–3 ml/min at 25 °C. The recorders were blinded to the group identity during recording and analysis.

Whole-cell patch-clamp recording. Neurons in the slice were visualized using a ×40 water-immersion objective on an upright microscope (BX51WI, Olympus, Tokyo, Japan) equipped with infrared differential interference contrast (IR-DIC) and an infrared camera connected to the video monitor. Whole-cell patch-clamp recordings were obtained from visually identified LC neurons. The recording pipettes (5-8 MΩ) were pulled by a horizontal micropipette puller (P-1000, Sutter Instrument) from borosilicate capillaries and filled with the following internal solution (in mM: 120 K-gluconate, 5 NaCl, 10 KCL, 1 $CaCl_2{\cdot}2H_2O$, 2 $MgCl_2{\cdot}6H_2O$, 11 EGTA, 10 HEPES, 2 Mg-ATP, and 1 Li-GTP, pH was adjusted to 7.3 with Tris-base). A 3 minutes equilibration period was allowed to reach the steady state after whole cell access was established. The resting membrane potential was continuously recorded with I = 0 current-clamp mode. To measure excitability of LC neurons, the action potential (AP) current threshold was tested using a series of 500 ms hyper- and depolarizing current injections in 10 pA steps ranging from −40 to 100 pA. The current that induced the first AP was defined as threshold current and the number of APs induced by each depolarizing current was recorded. The membrane potential was held at −70 mV for recording spontaneous excitatory postsynaptic currents (sEPSCs) with voltage clamp mode. Membrane voltage and current were amplified using MultiClamp 700B (Molecular Devices, Sunnyvale, Calif, USA), filtered at 2 kHz and digitized at 10 kHz. Data were acquired using pClamp 10.7 software (Molecular Devices, Sunnyvale, Calif, USA). Neurons were discarded if the access or input resistance changed by more than 20%.

Biocytin diffusion and post-hoc immunofluorescence staining. To visualize the recorded neurons, biocytin was used to be dissolved into the intracellular solution. After recording the brain slices, stay in whole-cell mode last for more than 10 minutes to allow the biocytin to diffuse out of the electrode into the recorded neuron. After biocytin diffusion, the electrode must be slowly retracted to reseal the neuron. Then, brain slices were fixed in 4% PFA for 1 hour. Thereafter, brain slices were washed with PBS three times and were permeabilized in 1% Triton-X100/PBS for 30 minutes. After blocking, brain slices were incubated in TH (1:1000, ab134461, Abcam) overnight. The sections were then incubated with fluorescence conjugated secondary antibodies (1:1000, Abcam) and Streptavidin-Cy3 (1:200, S6402, Sigma) at room temperature for 1.5 hours.

Optical-fiber-based Ca^{2+} signal recording

An optical fiber (RWD Life Science, 200um core, 0.39 NA, OD 1.25 mm) was inserted into the sites where the virus was injected. Optical-fiber-based Ca^{2+} recordings were achieved using a multichannel fiber photometry device (RWD Life Science, R820). Yellow light was delivered at 585 nm in a train of 15-ms light pulses at 20 Hz to evoke neuronal activities of downstream rMR neurons. The indicator of the sensor emitted a 470 nm laser to excite GCaMP8s fluorescence, which was used to measure the activity of the targeted neuron, and the 410 nm laser served as a control light.

Drug administration

For chemical denervation of hepatic sympathetic nerve, 6-Hydroxydopamine hydrobromide (6-OHDA) (HY-B1081A, MedChemExpress) was administered by intraperitoneal (i.p.) injection of 100 mg/kg. For mice with CSD model, 6-OHDA was injected intraperitoneally for 5 consecutive days before the beginning of the model, followed by 3 times per week to ensure continued denervation. The drug was dissolved in a saline solution containing 0.1% ascorbic acid to prevent oxidation.

For ICI 118,551 (HY-13951, MedChemExpress), ADRB2 antagonist was diluted in saline and administered i.p. at the dosage of 10 mg/kg. To sustainedly block the effects of ADRB2, ICI 118,551 was administered 30 minutes before everyday stress model.

For formoterol (HY-B0010, MedChemExpress), the ADRB2 agonist, was diluted in saline and administered i.p. at the dosage of 1 mg/kg. For sustained activation of ADRB2, formoterol was administered once daily.

For blocking corticosterone biosynthesis in the adrenal gland, metyrapone (HY-B1232, MedChemExpress) was administered by intraperitoneal (i.p.) injection of 80 mg/kg. The metyrapone was administered every day during the CSD conditions. Serum corticosterone levers are examined after sample collection.

Enzyme-linked immunosorbent assay (ELISA)

The level of noradrenaline (BA E-5200R, LDN, Germany) in liver tissue and levels of IL-6 (GEM0001-96T, Servicebio) and TNF-α (GEM0004-96T, Servicebio) in liver tissue and serum were detected by ELISA kits according to the manufacturers' instructions.

Flow cytometry

Liver immune cells were isolated from livers of 70% PHx mice and purified by centrifugation at 850 ×g with Percoll (GE Healthcare, USA). Residual red blood cells were lysed by Lysing Buffer (BD Biosciences, USA). Then liver immune cells were incubated with following primary antibodies for 30 minutes at 4°C: CD45, CD11b, LY6C, F4/80, LY6G, CD3, B220 (Biolegend). Cells were incubated on ice with the primary antibodies for 30 min. The cells were counted on the FACS Verse cell sorter (BD Biosciences) and analyzed using FlowJo software (TreeStar).

Quantification and statistical analysis

All data are presented as the mean ± SEM of at least three biological replicates per group. Statistical analysis was performed using GraphPad Prism 9.0 (GraphPad Software, San Diego, CA, USA). To compare differences between the two groups, the paired or unpaired Student's *t*-test was used. For multiple group comparisons, One-way or Two-way ANOVA followed by Tukey's or Bonferroni's post hoc test was used. Survival curves were compared using the log-rank (Mantel–Cox) test. Differences were considered statistically significant when a *p* value was lower than 0.05. All the details of the experiments can be found in the figure legends.

Reporting summary

Further information on research design is available in the Nature Portfolio Reporting Summary linked to this article.

Data availability

There are no restrictions on data availability in the manuscript. Source data are provided with this paper.

Code availability

Custom made codes for photometry data export and animal route tracking are available from the corresponding authors upon request.

References

1. Michalopoulos, G. K. & Bhushan, B. Liver regeneration: biological and pathological mechanisms and implications. *Nat. Rev. Gastroenterol. Hepatol.* **18**, 40–55 (2021).
2. Forbes, S. J. & Newsome, P. N. Liver regeneration - mechanisms and models to clinical application. *Nat. Rev. Gastroenterol. Hepatol.* **13**, 473–485 (2016).
3. van Mierlo, K. M., Schaap, F. G., Dejong, C. H. & Olde Damink, S. W. Liver resection for cancer: New developments in prediction, prevention and management of postresectional liver failure. *J. Hepatol.* **65**, 1217–1231 (2016).
4. Campana, L., Esser, H., Huch, M. & Forbes, S. Liver regeneration and inflammation: from fundamental science to clinical applications. *Nat. Rev. Mol. Cell Biol.* **22**, 608–624 (2021).
5. Mao, S. A., Glorioso, J. M. & Nyberg, S. L. Liver regeneration. *Transl. Res* **163**, 352–362 (2014).
6. O'Connor, D. B., Thayer, J. F. & Vedhara, K. Stress and Health: A Review of Psychobiological Processes. *Annu Rev. Psychol.* **72**, 663–688 (2021).
7. Liu, T. et al. Environmental eustress promotes liver regeneration through the sympathetic regulation of type 1 innate lymphoid cells to increase IL-22 in mice. *Hepatology* **78**, 136–149 (2023).
8. Liu, C. et al. Environmental eustress modulates beta-ARs/CCL2 axis to induce anti-tumor immunity and sensitize immunotherapy against liver cancer in mice. *Nat. Commun.* **12**, 5725 (2021).
9. Russell, G. & Lightman, S. The human stress response. *Nat. Rev. Endocrinol.* **15**, 525–534 (2019).
10. Zou, H. et al. Economic Burden and Quality of Life of Hepatocellular Carcinoma in Greater China: A Systematic Review. *Front Public Health* **10**, 801981 (2022).
11. Ji, W., Sang, C., Zhang, X., Zhu, K. & Bo, L. Personality, Preoperative Anxiety, and Postoperative Outcomes: A Review. *Int J. Environ. Res Public Health* **19**, 12162 (2022).
12. Mohamed, S., Sabki, Z. A. & Zainal, N. Z. Depression and psychosocial correlates of liver transplant candidates: a systematic review. *Asia Pac. Psychiatry* **6**, 447–453 (2014).
13. Russ, T. C. et al. Association Between Psychological Distress and Liver Disease Mortality: A Meta-analysis of Individual Study Participants. *Gastroenterology* **148**, 958–966 e954 (2015).
14. Ulrich-Lai, Y. M. & Herman, J. P. Neural regulation of endocrine and autonomic stress responses. *Nat. Rev. Neurosci.* **10**, 397–409 (2009).
15. Kiba, T., Tanaka, K., Numata, K., Hoshino, M. & Inoue, S. Facilitation of liver regeneration after partial hepatectomy by ventromedial hypothalamic lesions in rats. *Pflug. Arch.* **428**, 26–29 (1994).
16. Kiba, T., Tanaka, K. & Inoue, S. Lateral hypothalamic lesions facilitate hepatic regeneration after partial hepatectomy in rats. *Pflug. Arch.* **430**, 666–671 (1995).
17. Matchett, B. J., Grinberg, L. T., Theofilas, P. & Murray, M. E. The mechanistic link between selective vulnerability of the locus coeruleus and neurodegeneration in Alzheimer's disease. *Acta Neuropathol.* **141**, 631–650 (2021).
18. Seo, D. O. et al. A locus coeruleus to dentate gyrus noradrenergic circuit modulates aversive contextual processing. *Neuron* **109**, 2116–2130 e2116 (2021).
19. Chen, J. et al. A Vagal-NTS Neural Pathway that Stimulates Feeding. *Curr. Biol.* **30**, 3986–3998.e3985 (2020).
20. Fukushima, A., Kataoka, N. & Nakamura, K. An oxytocinergic neural pathway that stimulates thermogenic and cardiac sympathetic outflow. *Cell Rep.* **40**, 111380 (2022).
21. Nakamura, K. et al. Identification of sympathetic premotor neurons in medullary raphe regions mediating fever and other thermoregulatory functions. *J. Neurosci.* **24**, 5370–5380 (2004).
22. Jiao, Y. et al. Molecular identification of bulbospinal ON neurons by GPER, which drives pain and morphine tolerance. *J. Clin. Invest* **133**, e154588 (2023).
23. Dong, W. Y. et al. Brain regulation of gastric dysfunction induced by stress. *Nat. Metab.* **5**, 1494–1505 (2023).
24. Zhang, B. et al. Hyperactivation of sympathetic nerves drives depletion of melanocyte stem cells. *Nature* **577**, 676–681 (2020).
25. Liu, K. et al. Metabolic stress drives sympathetic neuropathy within the liver. *Cell Metab.* **33**, 666–675.e664 (2021).
26. Minagawa, M. et al. Intensive expansion of natural killer T cells in the early phase of hepatocyte regeneration after partial hepatectomy in mice and its association with sympathetic nerve activation. *Hepatology* **31**, 907–915 (2000).
27. Hurr, C., Simonyan, H., Morgan, D. A., Rahmouni, K. & Young, C. N. Liver sympathetic denervation reverses obesity-induced hepatic steatosis. *J. Physiol.* **597**, 4565–4580 (2019).
28. Reiche, E. M., Nunes, S. O. & Morimoto, H. K. Stress, depression, the immune system, and cancer. *Lancet Oncol.* **5**, 617–625 (2004).
29. Wynn, T. A. & Vannella, K. M. Macrophages in Tissue Repair, Regeneration, and Fibrosis. *Immunity* **44**, 450–462 (2016).
30. Jia, D. et al. Interleukin-35 Promotes Macrophage Survival and Improves Wound Healing After Myocardial Infarction in Mice. *Circ. Res.* **124**, 1323–1336 (2019).
31. Tacke, F. & Zimmermann, H. W. Macrophage heterogeneity in liver injury and fibrosis. *J. Hepatol.* **60**, 1090–1096 (2014).
32. Sun, H. et al. Ceramides and sphingosine-1-phosphate mediate the distinct effects of M1/M2-macrophage infusion on liver recovery after hepatectomy. *Cell Death Dis.* **12**, 324 (2021).

33. Cruz-Pereira, J. S., Rea, K., Nolan, Y. M., O'Leary, O. F., Dinan, T. G. & Cryan, J. F. Depression's Unholy Trinity: Dysregulated Stress, Immunity, and the Microbiome. *Annu Rev. Psychol.* **71**, 49–78 (2020).
34. Zhao, Y. et al. Disruption of Circadian Rhythms by Shift Work Exacerbates Reperfusion Injury in Myocardial Infarction. *J. Am. Coll. Cardiol.* **79**, 2097–2115 (2022).
35. Al Khatib, H. K., Harding, S. V., Darzi, J. & Pot, G. K. The effects of partial sleep deprivation on energy balance: a systematic review and meta-analysis. *Eur. J. Clin. Nutr.* **71**, 614–624 (2017).
36. Mavanji, V., Teske, J. A., Billington, C. J. & Kotz, C. M. Partial sleep deprivation by environmental noise increases food intake and body weight in obesity-resistant rats. *Obes. (Silver Spring)* **21**, 1396–1405 (2013).
37. McAlpine, C. S. et al. Sleep modulates haematopoiesis and protects against atherosclerosis. *Nature* **566**, 383–387 (2019).
38. Gu, Y., Zhang, W., Hu, Y., Chen, Y. & Shi, J. Association between nonalcoholic fatty liver disease and depression: A systematic review and meta-analysis of observational studies. *J. Affect Disord.* **301**, 8–13 (2022).
39. Yimlamai, D. et al. Hippo pathway activity influences liver cell fate. *Cell* **157**, 1324–1338 (2014).
40. Jung, Y. S. et al. TMEM9-v-ATPase Activates Wnt/β-Catenin Signaling Via APC Lysosomal Degradation for Liver Regeneration and Tumorigenesis. *Hepatology* **73**, 776–794 (2021).
41. Chan, K. L., Poller, W. C., Swirski, F. K. & Russo, S. J. Central regulation of stress-evoked peripheral immune responses. *Nat. Rev. Neurosci.* **24**, 591–604 (2023).
42. Kivimäki, M., Bartolomucci, A. & Kawachi, I. The multiple roles of life stress in metabolic disorders. *Nat. Rev. Endocrinol.* **19**, 10–27 (2023).
43. Yang, F. et al. A GABAergic neural circuit in the ventromedial hypothalamus mediates chronic stress-induced bone loss. *J. Clin. Invest* **130**, 6539–6554 (2020).
44. Zsombok, A., Desmoulins, L. D. & Derbenev, A. V. Sympathetic circuits regulating hepatic glucose metabolism, where we stand. *Physiol. Rev.* **104**, 85–101 (2023).
45. Ohtake, M., Sakaguchi, T., Yoshida, K. & Muto, T. Hepatic branch vagotomy can suppress liver regeneration in partially hepatectomized rats. *HPB Surg.* **6**, 277–286 (1993).
46. Iwai, M. & Shimazu, T. Alteration in sympathetic nerve activity during liver regeneration in rats after partial hepatectomy. *J. Auton. Nerv. Syst.* **41**, 209–214 (1992).
47. Lelou, E. et al. The Role of Catecholamines in Pathophysiological Liver Processes. *Cells* **11**, 1021 (2022).
48. Oben, J. A. et al. Sympathetic nervous system inhibition increases hepatic progenitors and reduces liver injury. *Hepatology* **38**, 664–673 (2003).
49. Sharma, D. & Farrar, J. D. Adrenergic regulation of immune cell function and inflammation. *Semin Immunopathol.* **42**, 709–717 (2020).
50. Cruise, J. L., Houck, K. A. & Michalopoulos, G. K. Induction of DNA synthesis in cultured rat hepatocytes through stimulation of alpha 1 adrenoreceptor by norepinephrine. *Science* **227**, 749–751 (1985).
51. Thomas, P., Hayashi, H., Zimmer, R. & Forse, R. A. Regulation of cytokine production in carcinoembryonic antigen stimulated Kupffer cells by beta-2 adrenergic receptors: implications for hepatic metastasis. *Cancer Lett.* **209**, 251–257 (2004).
52. Ozaki, M. Cellular and molecular mechanisms of liver regeneration: Proliferation, growth, death and protection of hepatocytes. *Semin Cell Dev. Biol.* **100**, 62–73 (2020).
53. Taub, R. Liver regeneration: from myth to mechanism. *Nat. Rev. Mol. Cell Biol.* **5**, 836–847 (2004).
54. Schmidt-Arras, D. & Rose-John, S. IL-6 pathway in the liver: From physiopathology to therapy. *J. Hepatol.* **64**, 1403–1415 (2016).
55. Liu, W. Z. et al. Identification of a prefrontal cortex-to-amygdala pathway for chronic stress-induced anxiety. *Nat. Commun.* **11**, 2221 (2020).
56. Wright, K. P. Jr et al. Influence of sleep deprivation and circadian misalignment on cortisol, inflammatory markers, and cytokine balance. *Brain Behav. Immun.* **47**, 24–34 (2015).
57. Jiang, W. et al. Chronic restraint stress promotes hepatocellular carcinoma growth by mobilizing splenic myeloid cells through activating beta-adrenergic signaling. *Brain Behav. Immun.* **80**, 825–838 (2019).
58. Gao, T. et al. Role of melatonin in sleep deprivation-induced intestinal barrier dysfunction in mice. *J. Pineal Res* **67**, e12574 (2019).
59. Zhu, L. et al. Remifentanil preconditioning promotes liver regeneration via upregulation of beta-arrestin 2/ERK/cyclin D1 pathway. *Biochem Biophys. Res Commun.* **557**, 69–76 (2021).
60. Mitchell, C. & Willenbring, H. A reproducible and well-tolerated method for 2/3 partial hepatectomy in mice. *Nat. Protoc.* **3**, 1167–1170 (2008).

Acknowledgements

This study was supported by the National Natural Science Foundation of China (No. 82371517 to L.-Q.Y., 82270916 to P.G., U23A20508 to L.-Q.Y., 32030043 to W.-F.Y., 82371478 to Y.-F.J., 82371536 to S.Z., 81771185 to L.-Q.Y., 81800748 to P.G.), Pudong New Area Health Commission Research Project (No. PW2022D-01 to L.-Q.Y.), the Fundamental Research Funds for the Central Universities (No. 24X010202059 to W.-F.Y.), and Shanghai Engineering Research Center of Peri-operative Organ Support and Function Preservation (No. 20DZ2254200 to W.-F.Y.). We thank Prof. Wei L Shen from ShanghaiTech University for kindly gifting *Th*-Cre mice. We also would like to express their gratitude to EditSprings (https://www.editsprings.cn) for the expert linguistic services provided.

Author contributions

L.-Q.Y., P.G., W.-F.Y. and Y.-F.J. designed the experiments. Y.-Y.Z., X.-Q.L., P.G., Y.-F.J. and D.Y. performed the experiments and analyzed the data. Y.-Y.Z., P.G., L.-Q.Y. and X.-Q.L. wrote the manuscript. Y.-F.J., W.-F.Y., Z.-Y.L., L.Z., Y.-X.L., S.-Q.Y., Q.-F.L., S.-H.X., D.T. and S.Z. provided critical suggestions and revised the manuscript. P.G., L.-Q.Y., W.-F.Y., Y.-Y.Z. and Y.-F.J. completed the final review and submitted the manuscript. All authors contributed to the article and approved the submitted version.

Competing interests

The authors declare no competing interests.

Additional information

Supplementary information The online version contains supplementary material available at https://doi.org/10.1038/s41467-024-54827-5.

Correspondence and requests for materials should be addressed to Weifeng Yu, Po Gao or Liqun Yang.

Peer review information *Nature Communications* thanks Jing Yang, Zhi Zhang and the other, anonymous, reviewer(s) for their contribution to the peer review of this work. A peer review file is available.